Computer Methods in Applied Mechanics and Engineering 112 (1994) 253–282
North-Holland

Massively parallel finite element computation of incompressible flows involving fluid–body interactions*

S. Mittal and T.E. Tezduyar

Department of Aerospace Engineering and Mechanics, Army High Performance Computing Research Center and Supercomputer Institute, University of Minnesota, 1200 Washington Avenue South, Minneapolis, MN 55415, USA

Received 4 December 1992
Revised manuscript received 10 December 1992

We describe our massively parallel finite element computations of unsteady incompressible flows involving fluid–body interactions. These computations are based on the Deforming-Spatial-Domain/Stabilized-Space-Time (DSD/SST) finite element formulation. Unsteady flows past a stationary NACA 0012 airfoil are computed for Reynolds numbers 1000, 5000 and 100 000. Significantly different flow patterns are observed for these three cases. The method is then applied to computation of the dynamics of an airfoil falling in a viscous fluid under the influence of gravity. It is observed that the location of the center of gravity of the airfoil plays an important role in determining its pitch stability. Computations are reported also for simulation of the dynamics of a two-dimensional 'projectile' that has a certain initial velocity. Specially designed mesh moving schemes are employed to eliminate the need for remeshing. All these computations were carried out on the Thinking Machines CM-200 and CM-5 supercomputers, with major speed-ups compared to traditional supercomputers. The implicit equation systems arising from the finite element discretizations of these large-scale problems are solved iteratively by using the GMRES update technique with diagonal preconditioners. The finite element formulations and their parallel implementations assume unstructured meshes.

1. Introduction

We present our numerical results for unsteady flows involving fluid–body interactions. The equations governing the fluid flow and the motion of the rigid body are solved using the stabilized space–time finite element method. Massively parallel implementation of these formulations on the Thinking Machines CM-200 and CM-5 supercomputers are employed to compute solutions to these large-scale problems. In the space–time formulation, the finite element interpolation functions vary both spatially and temporally. This fact can be exploited to solve problems that involve moving boundaries and interfaces. It was first shown by Tezduyar et al. [1, 2] that the stabilized space–time finite element formulation can be effectively applied to fluid dynamics computations involving moving boundaries and interfaces. They introduced the DSD/SST (Deforming-Spatial-Domain/Stabilized-Space-Time) procedure and successfully applied it to several unsteady incompressible flow problems involving moving boundaries and interfaces, such as free-surface flows, liquid drops, two-liquid flows and flows with drifting cylinders. Later, Mittal and Tezduyar [3] applied this method to solve flows past oscillating cylinders and airfoils. A description of the massively parallel implementation of the stabilized space–time method along with several example problems can be found in the article by Behr et al. [4]. The stabilization of the numerical method is achieved by adding a series of stabilizing terms to the Galerkin

Correspondence to: Professor Tayfun E. Tezduyar, Supercomputer Institute, 1200 Washington Avenue South, Minneapolis, MN 55415, USA. Tel.: (612) 626-8067; Fax: (612) 624-8861.

* This research was sponsored by NASA-JSC under grant NAG 9-449, by NSF under grant MSM-8796352, by ALCOA Foundation, and by ARPA under NIST contract GONANB2D1272. Partial support for this work has also come from the Army Research Office contract number DAAL03-89-C-0038 with the Army High Performance Computing Research Center at the University of Minnesota.

formulation. These terms can be obtained by minimizing the sum of the squared residual of the momentum equation integrated over each element domain. This kind of stabilization is known as the Galerkin/least-squares (GLS) stabilization. This approach has been successfully applied to Stokes flows [5], compressible flows [6, 7], and incompressible flows at finite Reynolds numbers [1, 2, 8, 9]. To reduce the computational costs associated with the space–time method, iterative solution strategies are employed. The implicit equation systems arising from the finite element discretizations of the problems are solved by using the GMRES [4, 10] (Generalized Minimal Residual) update technique with diagonal preconditioners. The finite element formulations and their parallel implementations employed in this work assume unstructured meshes.

The first problem considered in this paper is the computation of laminar flow over a flat plate at Reynolds number 1 000 000. Computation of flows at high Reynolds numbers has always been challenging in fluid dynamics. The difficulties posed by these flows are twofold. Firstly, because of the dominance of the advection terms in the governing equations, a standard Galerkin formulation of the problem can lead to spurious node-to-node oscillations. The use of stabilization techniques like the SUPG [11, 12] (Streamline-upwind/Petrov-Galerkin) or GLS can prevent such oscillations. The second kind of difficulty associated with the computation of high Reynolds number flows is due to the presence of thin boundary layers in the solutions. If these layers are not adequately resolved, one can get quite inaccurate solutions. In certain cases, if the formulation is not stable enough, the unresolved layers may even lead to spurious node-to-node oscillations. These oscillations could then get advected downstream and corrupt the solution in the entire computational domain. Computation of the laminar flow over a flat plate at Reynolds number 1 000 000 demonstrates the robustness of our formulations and provides an estimate of the resolution of the mesh needed near the flat plate. The computed results match very well with the solution given by Blasius [13] for a laminar boundary layer. This estimate of the 'element length' is later used to compute flow past a stationary airfoil at Reynolds number 100 000.

Next, results are presented for flows past a stationary NACA 0012 airfoil at Reynolds numbers 1000, 5000 and 100 000. Our computations indicate that the flows at Reynolds numbers 1000 and 5000 are temporally periodic. At Reynolds number 100 000, the flow ceases to be temporally periodic. Interesting differences exist between the flow patterns for all three flows. We do realize that, in reality, the flows at such high Reynolds are turbulent. Our goal here is to demonstrate that our formulations are robust enough to handle numerical challenges posed by such flows.

Having computed flows past stationary objects, we apply the DSD/SST method to flows involving moving airfoils and projectiles. First, the dynamics of an airfoil freely falling under the action of gravity is presented for two different mass distributions of the airfoil. It is observed that the location of the center of gravity of the airfoil plays an important role in determining its pitch stability. The final computation is the simulation of a two-dimensional 'projectile', falling under gravity, that has a certain initial velocity. All these problems involve large displacements (both linear and angular) of rigid bodies. By employing specially designed mesh moving schemes, we are able to handle these displacements without any remeshing. Therefore, our solutions are free of projection errors associated with remeshing. Avoiding remeshing also aids us in utilizing the massively parallel machines efficiently.

The governing equations

2.1. The Navier–Stokes equations

Let Ω_t in $R^{n_{sd}}$ be the spatial domain at time $t \in (0, T)$, where n_{sd} is the number of space dimensions. Let Γ_t denote the boundary of Ω_t. We consider the following velocity–pressure formulation of the Navier–Stokes equations governing unsteady incompressible flows:

$$\rho\left(\frac{\partial \boldsymbol{u}}{\partial t} + \boldsymbol{u} \cdot \nabla \boldsymbol{u}\right) - \nabla \cdot \boldsymbol{\sigma} = 0 \quad \text{on } \Omega_t \quad \forall t \in (0, T), \tag{1}$$

$$\nabla \cdot \boldsymbol{u} = 0 \quad \text{on } \Omega_t \quad \forall t \in (0, T \tag{2}$$

where ρ and $\boldsymbol{u}$ are the density and velocity, and $\boldsymbol{\sigma}$ is the stress tensor given as

$$\boldsymbol{\sigma}(p, \boldsymbol{u}) = -p\boldsymbol{I} + 2\mu\boldsymbol{\epsilon}(\boldsymbol{u})$$

with

$$\boldsymbol{\epsilon}(\boldsymbol{u}) = \tfrac{1}{2}(\nabla\boldsymbol{u} + (\nabla\boldsymbol{u})^{t})$$

Here p and μ are the pressure and the dynamic viscosity, and $\boldsymbol{I}$ is the identity tensor. The part of the boundary at which the velocity is assumed to be specified is denoted by $(\Gamma_t)_g$:

$$\boldsymbol{u} = \boldsymbol{g} \quad \text{on } (\Gamma_t)_g \quad \forall t \in (0, T)$$

The 'natural' boundary conditions associated with (1) are the conditions on the stress components, and these are the conditions assumed to be imposed at the remaining part of the boundary:

$$\boldsymbol{n} \cdot \boldsymbol{\sigma} = \boldsymbol{h} \quad \text{on } (\Gamma_t)_h \quad \forall t \in (0, T)$$

The homogeneous version of (6), which corresponds to the 'traction-free' (i.e., zero normal and shear stress) conditions, is often imposed at the outflow boundaries. As initial condition, a divergence-free velocity field $\boldsymbol{u}_0(\boldsymbol{x})$ is specified over the domain Ω_t at $t = 0$:

$$\boldsymbol{u}(\boldsymbol{x}, 0) = \boldsymbol{u}_0(\boldsymbol{x}) \quad \text{on } \Omega_0$$

2.2. Equations of motion for a rigid body in two dimensions

Consider the motion of a rigid body in a two-dimensional space. The rigid body is assumed to be attached to a linear spring and a dash pot for each of its degree of freedom of motion. Let v_x and v_y represent the linear velocity components of the center of gravity of the body (G) and let Θ be its angular velocity. Let f_x and f_y be the two components of the force and J the torque acting on the body. These forces consist of the contributions from the surface traction (includes fluid forces) and body forces acting on the body. The linear displacements are represented by δ_x and δ_y while θ represents the angular displacement.

The equation of motion for the body is given as

$$\boldsymbol{ma} + \boldsymbol{cv} + \boldsymbol{k\delta} = \boldsymbol{f}\,,$$

where $\boldsymbol{m}$, $\boldsymbol{c}$, $\boldsymbol{k}$ and $\boldsymbol{f}$ are, respectively, the mass matrix, damping matrix, stiffness matrix and the force vector; $\boldsymbol{a}$, $\boldsymbol{v}$ and $\boldsymbol{\delta}$ are the acceleration, velocity and the displacement vectors, respectively, associated with the rigid body. The expanded form of these matrices and vectors are given below.

$$\boldsymbol{m} = \begin{Bmatrix} m & 0 & 0 \\ 0 & m & 0 \\ 0 & 0 & I \end{Bmatrix}$$

where m is the mass of the body and I is the polar moment of inertia about an axis passing through the center of gravity of the body. In the relations given below, the subscripts x and y refer to the quantities related to the x and y directions, respectively. The subscript θ refers to the quantities related to the angular motion of the body.

$$\boldsymbol{c} = \begin{Bmatrix} c_x & 0 & 0 \\ 0 & c_y & 0 \\ 0 & 0 & c_\theta \end{Bmatrix}$$

$$\boldsymbol{k} = \begin{Bmatrix} k_x & 0 & 0 \\ 0 & k_y & 0 \\ 0 & 0 & k_\theta \end{Bmatrix}$$

$$f = \begin{Bmatrix} f_x \\ f_y \\ J \end{Bmatrix} \tag{12}$$

(13)

$$v = \delta\ , \tag{14}$$

$$v = \begin{Bmatrix} v_x \\ v_y \\ \Theta \end{Bmatrix} \tag{15}$$

$$\delta = \begin{Bmatrix} \delta_x \\ \delta_y \\ \theta \end{Bmatrix} \tag{16}$$

It should be noted that in (8) the damping matrix c consists of structural damping only. The fluid damping comes into the equations of motion through the force vector f which includes the surface traction on the body. As initial condition, for (8), displacements and velocities at $t = 0$ are specified for the rigid body:

$$v(0) = v_0\ , \tag{17}$$

$$\delta(0) = \delta_0 \tag{18}$$

If one is interested in studying the motion of a body that is not constrained by any springs or dash pots, (8) can still be used if the terms associated with the stiffness and damping are dropped.

Finite element formulations

3.1. The space–time formulation with the Galerkin/least-squares stabilization

The conventional finite element formulations for unsteady problems usually involve a finite difference type of discretization in time. In the space–time formulation, the finite element interpolation functions vary both spatially and temporally. This fact can be exploited to solve problems that involve moving boundaries and interfaces.

In the space–time finite element formulation, the time interval $(0, T)$ is partitioned into subintervals $I_n = (t_n, t_{n+1})$, where t_n and t_{n+1} belong to an ordered series of time levels $0 = t_0 < t_1 < \cdots < t_N = T$. In this formulation, the spatial domains at various time levels are allowed to vary. We let $\Omega_n = \Omega_{t_n}$ and $\Gamma_n = \Gamma_{t_n}$, and define the space–time slab Q_n as the space–time domain enclosed by the surfaces Ω_n, Ω_{n+1} and P_n. Here P_n, the lateral surface of Q_n, is the surface described by the boundary Γ, as t traverses I_n. Similar to the way it was represented in (5) and (6), P_n is decomposed into $(P_n)_g$ and $(P_n)_h$ with respect to the type of boundary condition being imposed.

Finite element discretization of a space–time slab Q_n is achieved by dividing it into elements Q_n^e, $e = 1, 2, \ldots, (n_{el})_n$, where $(n_{el})_n$ is the number of elements in the space–time slab Q_n. Associated with this discretization, for each space–time slab we define the following finite element interpolation function spaces for the velocity and pressure:

$$= \{u^h \mid u^h \in [H^{1h}(Q_n)]^{n_{sd}},\ u^h \doteq g^h \text{ on } (P_n)_g \tag{19}$$

$$= \{w^h \mid w^h \in [H^{1h}(Q_n)]^{n_{sd}},\ w^h \doteq \mathbf{0} \text{ on } (P_n)_g\}\ , \tag{20}$$

$$(S_p^h)_n = \{q^h \mid q^h \in H^{1h}(Q_n)\} \tag{21}$$

$$V \quad q \quad q \quad H \quad Q$$

Here $H^{1h}(Q_n)$ represents the finite-dimensional function space over the space–time slab Q_n. This space is formed by using, over the parent (element) domains, first-order polynomials in space and time. It is also possible to use zeroth-order polynomials in time. In either case, globally, the interpolation functions are continuous in space but discontinuous in time.

The space–time formulation of (1)–(7) can be written as follows: start with

$$(u^n)$$

sequentially for $Q \quad Q \quad Q_N$ given $(u$ find $u^h \quad (S_u^h)_n$ and $p \quad S_p^h)_n$, such that $\forall w^h \in (V_u^h$ and $\forall q^h \in (V_n^h)_n$,

$$w \quad \rho\left(\frac{\partial u}{\partial t} \quad u \quad \nabla u^h\right) \mathrm{d}Q \qquad \varepsilon(w^n) : \sigma(p \quad u \quad \mathrm{d}Q$$

$$h \,\mathrm{d}P \quad q^h \nabla \cdot u^h \,\mathrm{d}Q \qquad (w \quad \rho((u \quad (u \quad \mathrm{d}\Omega$$

$$\sum^{n_{el})_n} \int_{Q_n^e} \rho \quad \rho\left(\frac{\partial w^n}{\partial t} + u^h \cdot \nabla w^h\right) \quad \nabla \cdot \sigma(q^h, w$$

$$\rho\left(\frac{\partial u'}{\partial t} \quad u^h \cdot \nabla u\right) \quad \nabla \cdot \sigma(p \quad u \quad \mathrm{d}Q$$

$$\sum \int \delta\rho \nabla \cdot w^h \, \nabla \cdot u^h \,\mathrm{d}Q \quad 0$$

In the variational formulation given by (24), the following notation is used:

$$(u^h) \quad \lim u^h(t$$

$$\int_Q \quad) \,\mathrm{d}Q \quad \int \int \quad \mathrm{d}\Omega \,\mathrm{d}t$$

$$\int_P \quad) \,\mathrm{d}P \quad \int \quad \mathrm{d}\Gamma \,\mathrm{d}t$$

If we were in a standard finite element formulation, rather than a space–time one, the Galerkin formulation of (1)–(7) would have consisted of the first four integrals (their spatial versions) appearing in (24). In the space–time formulation, because the interpolation functions are discontinuous in time, the fully discrete equations can be solved one space–time slab at a time. The fifth integral in (24) enforces, weakly, the continuity of the velocity in time.

In (24), the series of integrals involving the coefficients τ and δ are the least-squares terms added to the Galerkin variational formulation to assure the numerical stability of the computations. This kind of stabilization of the Galerkin formulation is referred to as the Galerkin/least-squares (GLS) procedure, and can be considered as a generalization of the stabilization based on the streamline-upwind/Petrov-Galerkin (SUPG) and pressure-stabilizing/Petrov-Galerkin (PSPG) procedures employed for incompressible flows [12]. It is with such stabilization procedures that it is possible to use elements which have equal-order interpolation functions for velocity and pressure, and which are otherwise unstable. The coefficient τ used in this formulation is obtained by a simple multi-dimensional generalization of the optimal τ given in [7] for one-dimensional space–time formulation. The expression for the τ used in this formulation is

$$\tau = \left(\left(\frac{2\|u^h\|}{h} \right)^2 + \left(\frac{4\nu}{h^2} \right)^2 \right)^{-1/2} \tag{28}$$

where ν is the kinematic viscosity and h is the spatial element length. For derivation of τ for higher-order elements, see [14]. The expression for δ is very similar to that used in [15]; that is,

$$\delta = \tfrac{1}{2} h \|\boldsymbol{u}^h\| z \, , \tag{29}$$

where z is defined as

$$z = \begin{cases} \left(\frac{\mathrm{Re}_u}{3} \right), & \mathrm{Re}_u \leqslant 3 \, , \\ 1 \, , & \mathrm{Re}_u \geqslant 3 \, . \end{cases} \tag{30}$$

Here Re_u is the element Reynolds number defined as

$$\mathrm{Re}_u = \frac{\|\boldsymbol{u}^h\| h}{2\nu} \tag{31}$$

This form of z is the same as that used in [12]. It is important to realize that the stabilizing terms added involve the momentum equation as a factor. Therefore, despite these additional terms, an exact solution is still admissible to the variational formulation given by (24). Therefore, in this respect, our formulations are consistent.

3.2. Application to flows involving moving bodies

We now apply the space–time formulation to the equation of motion for a rigid body in two dimensions (8). If we perform the time integration of (8), we obtain

$$\begin{aligned} v_{n+1}^- = r^{-1} \Bigg[& \frac{\Delta t}{4} \left(m + \frac{\Delta t}{3} c \right) f_{n+1}^- + \frac{\Delta t}{4} m f_n^+ - \frac{\Delta t}{2} k \left(m + \frac{\Delta t}{6} c \right) \delta_n \\ & - \left(-\frac{1}{2} mm + \frac{\Delta t}{6} mc + \frac{\Delta t^2}{8} mk + \frac{\Delta t^3}{24} ck \right) v_n^- \Bigg] \end{aligned} \tag{32}$$

$$r = \frac{1}{2} mm + \frac{\Delta t}{3} mc + \left(\frac{1}{8} mk + \frac{1}{12} cc \right) \Delta t^2 + \frac{\Delta t^3}{24} ck \, . \tag{33}$$

The location of the center of gravity of the rigid body is updated by using the following relation:

$$\boldsymbol{\delta}_{n+1} = \boldsymbol{\delta}_n + \frac{\Delta t}{2} (\boldsymbol{v}_{n+1}^- + \boldsymbol{v}_n^-) \tag{34}$$

4. Numerical examples

4.1. Laminar boundary layer on a flat plate at Reynolds number 1 000 000

Our motivation to solve this problem is twofold. Firstly, we want to demonstrate the robustness of the stabilized space–time formulation in handling flow problems involving high Reynolds numbers. Flows at high Reynolds numbers are associated with thin boundary layers. In the computations, if these layers are not adequately resolved one can get quite inaccurate solutions, especially, if one is interested in the flow close to these layers. This leads us to the second motivation for solving this problem. Since analytical solution is available for laminar boundary layer on a flat plate, it is possible to estimate the minimum size of the elements close to the flat plate required to resolve the boundary layer adequately. In the next section, we use the same estimate of the element near the airfoil surface to compute flow past it at Reynolds number 100 000.

A flat plate with unit length forms the boundary B1–B2 of the computational domain (see Fig. 1). The inflow boundary B4–B5 is located at a distance of 0.5 from the leading edge of the flat plate. The inlet velocity is specified to be 1.0. Reynolds number is defined on the basis of the inlet velocity and the length of the plate. Symmetry boundary condition is applied on the top boundary B4–B3 and part of the lower boundary B1–B5, i.e., the horizontal component of the stress vector is set to zero while no flow is allowed across the two boundaries. The top boundary B4–B3 is located at a distance of 0.5 from the lower boundary B5–B2. Traction-free boundary condition is applied at the outflow boundary B2–B3. This boundary condition is not really consistent. Close to the wall, as the boundary layer leaves the domain, there are viscous stresses in the flow. A consistent way to treat this boundary condition has been discussed in [7]. All the computations reported in this section are for steady-state equations and are performed on a CRAY-2. Constant-in-time interpolation functions are used and a direct solver is employed to solve the equation system resulting from finite element discretization.

The local skin friction coefficient, C_f, on the surface of the plate is defined as

$$C_f = \frac{\mu\left(\frac{\partial u_1}{\partial x_2}\right)_{\text{wall}}}{0.5\rho U^2}$$

where U is the inlet velocity.

The Blasius solution for a laminar boundary layer [13] is

$$C_f = 0.664/\sqrt{R_x}$$

where $R_x = \rho U x/\mu$ and x is the distance measured from the leading edge of the plate.

As can be seen from (36), the solution for the flat plate involves a singularity at the leading edge. Therefore, a fairly fine mesh is used near the leading edge.

First, a convergence study, with respect to the size, in the vertical direction, of the first layer of elements on the plate, is performed. The mesh employed consists of 2046 nodes and 1950 elements. Figure 2 shows the variation of the local skin friction coefficient with the distance from the leading edge of the plate for four different mesh sizes. In the figure, the first element size in the vertical direction is

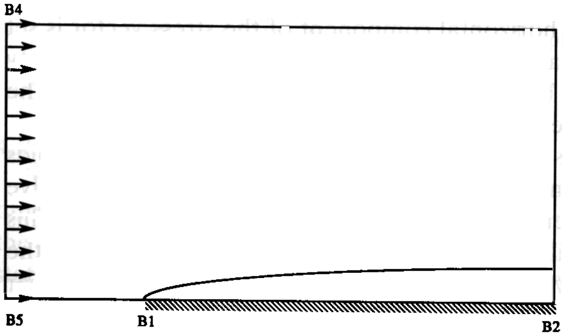

Fig. 1. Laminar boundary layer on a flat plate at Reynolds number 1 000 000: problem description.

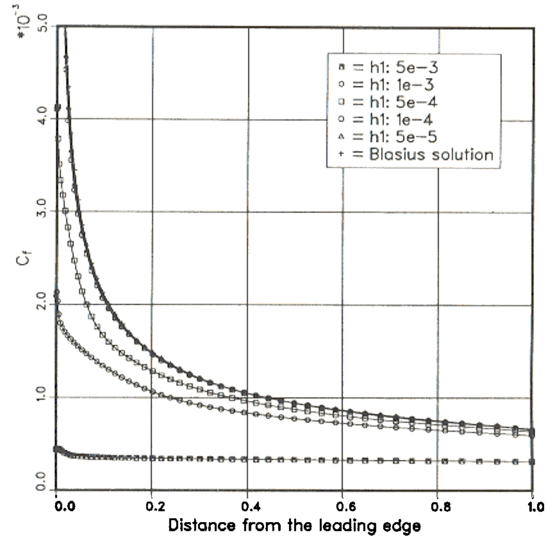

Fig. 2. Laminar boundary layer on a flat plate at Re = 1 000 000: local skin friction coefficient along the plate for different meshes with same number of elements (1950) but different 'element length'.

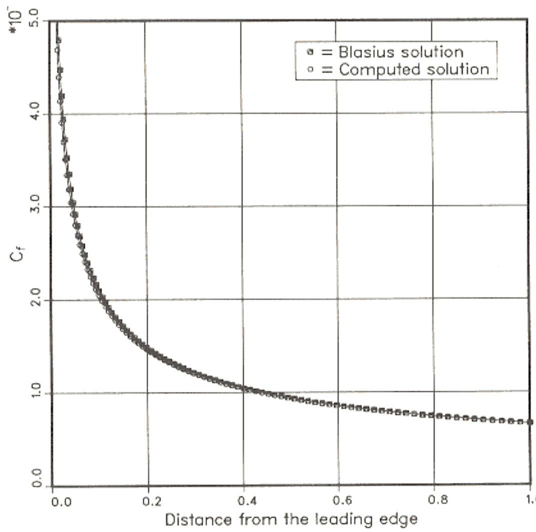

Fig. 3. Laminar boundary layer on a flat plate at Re = 1 000 000: local skin friction coefficient along the plate for a fine mesh with 8125 elements.

denoted by '$h1$'. Also shown in the same figure is the Blasius solution given by (36). We observe that the solutions given by the meshes with $h1 = 0.005$, 0.001 and 0.0005 are quite inaccurate. On the other hand, the solutions from the meshes with $h1 = 0.0001$ and 0.00005 give solutions very close to the Blasius solution. This demonstrates the need for the boundary layers to be resolved adequately, especially, if one is interested in the flow close to the walls.

Figure 3 shows the variation in C_f along the length of the plate for a finer mesh with $h1 = 0.0001$. This mesh has 8316 nodes and 8125 elements. We observe from Fig. 3 that the computed solution is in very good agreement with the Blasius solution (36). This fact justifies the use of a mesh with first element size of 0.0001 for computing the flow past a stationary airfoil at Reynolds number 100 000. Figure 4 shows the isobars and velocity vectors for the computed solution for the laminar boundary layer on a flat plate.

4.2. Flow past a stationary NACA 0012 airfoil at three different Reynolds numbers

The airfoil with unit chord length is located at the origin. The inflow boundary is located at 6 chord lengths upstream of the airfoil; the inflow velocity is 1.0. The angle of attack for the airfoil is 10°. The Reynolds number is based on the chord length of the airfoil and the free-stream velocity. The upper and lower boundaries are again located at 6 chord lengths from the airfoil. Symmetry boundary conditions are applied at these two boundaries, i.e., the horizontal component of the stress vector is set to zero while no flow is allowed across the two boundaries. The outflow boundary is located twenty chord lengths downstream of the airfoil. Stress-free boundary conditions are applied there. The computations are carried out for three Reynolds numbers: 1000, 5000 and 100 000.

Figure 5 shows a close-up of the finite element meshes employed for the computations. For Reynolds numbers 1000 and 5000, a mesh with 23 600 elements and 23 900 nodes is used. To adequately resolve the boundary layer around the airfoil at Reynolds number 100 000 we refine the mesh even further. This refinement is confined to the region close to the airfoil. The length of the layer of elements on the surface of the airfoil is based on the convergence analysis for the boundary layer on a flat plate. Far away, the mesh stays the same. This mesh consists of 26 600 elements and 26 900 nodes. Linear-in-time shape functions are used. The equation systems resulting from the implicit finite element formulations are solved iteratively using the GMRES technique with a diagonal preconditioner; a Krylov vector space of dimension 50 is used. Figure 6 shows the power spectra for the aerodynamic coefficients related to the airfoil as a result of our computations for the three Reynolds numbers.

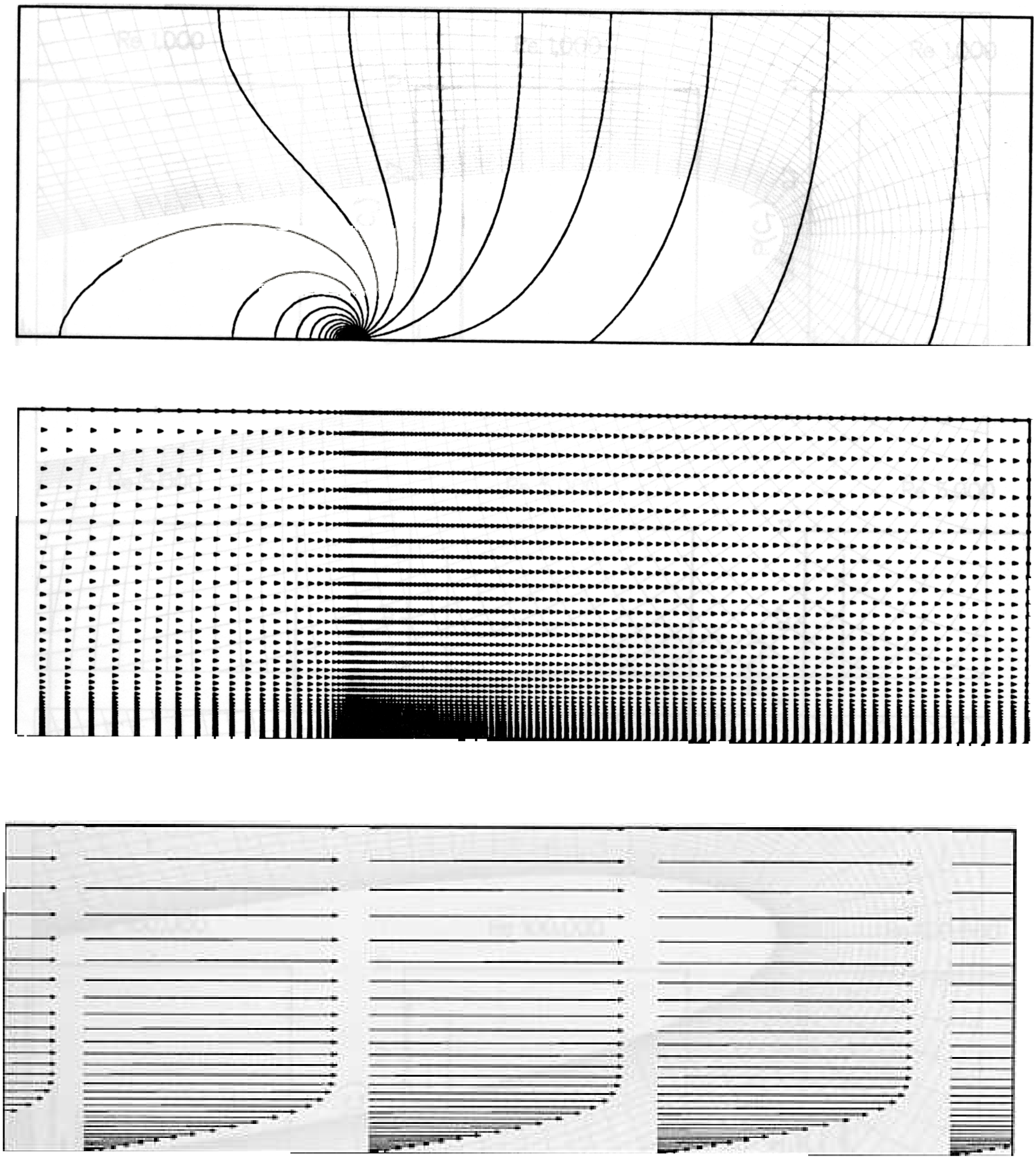

Fig. 4. Laminar boundary layer on a flat plate at Re = 1 000 000: velocity vectors and pressure.

4.2.1. Reynolds number 1000

The time step size is 0.01. The size of the first layer of elements around the airfoil is 0.002. At each time step approximately 142 000 equations are solved iteratively. Figure 7 shows the time histories of the lift, drag and torque coefficients acting on the airfoil. We observe that the flow reaches a periodic state. From Figure 6 we observe that the flow at Reynolds number 1000 has only one dominant frequency. The Strouhal number (based on the chord length and the free-stream velocity) is 0.862. Figure 8[1] shows a sequence of frames for the vorticity field during one period of the lift coefficient. The first, third and last frames correspond to the mean lift coefficient, while the second and fourth frames

[1]Figures 8–10, 12–14, 16–18, 21(a, b), 24(a, b) and 27 are given on pages 275–282.

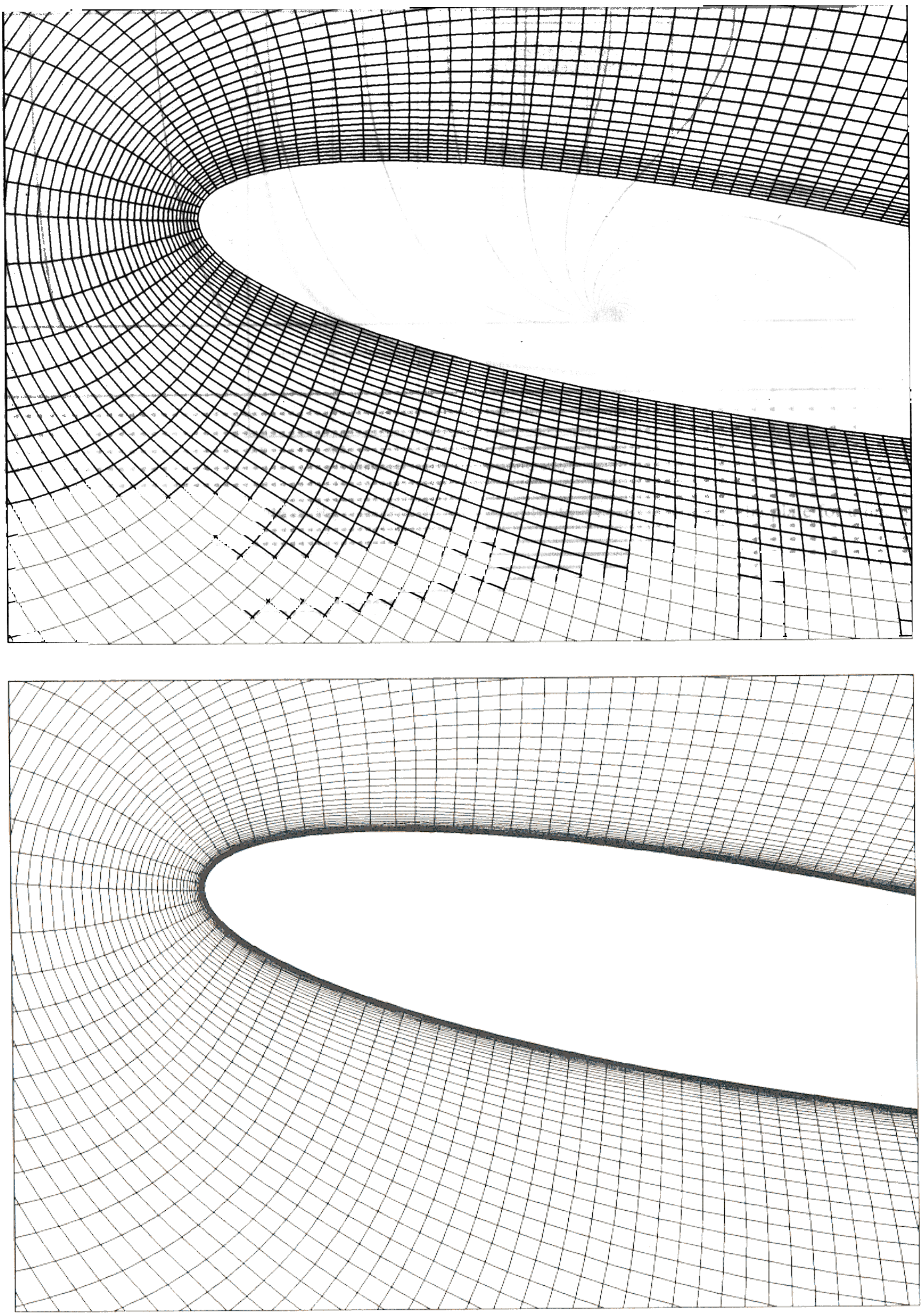

Fig. 5. Flow past a stationary NACA 0012 airfoil: finite element mesh close to the airfoil for Re = 1000 and 5000 (top) and for Re = 100 000 (bottom).

correspond, respectively, to the minimum and maximum values of the lift. Figures 9 and 10 show, respectively, a similar sequence of frames for the close-up of the vorticity field and stream function. We observe that, at this Reynolds number, the wake behind the airfoil looks very similar to that behind a cylinder [12].

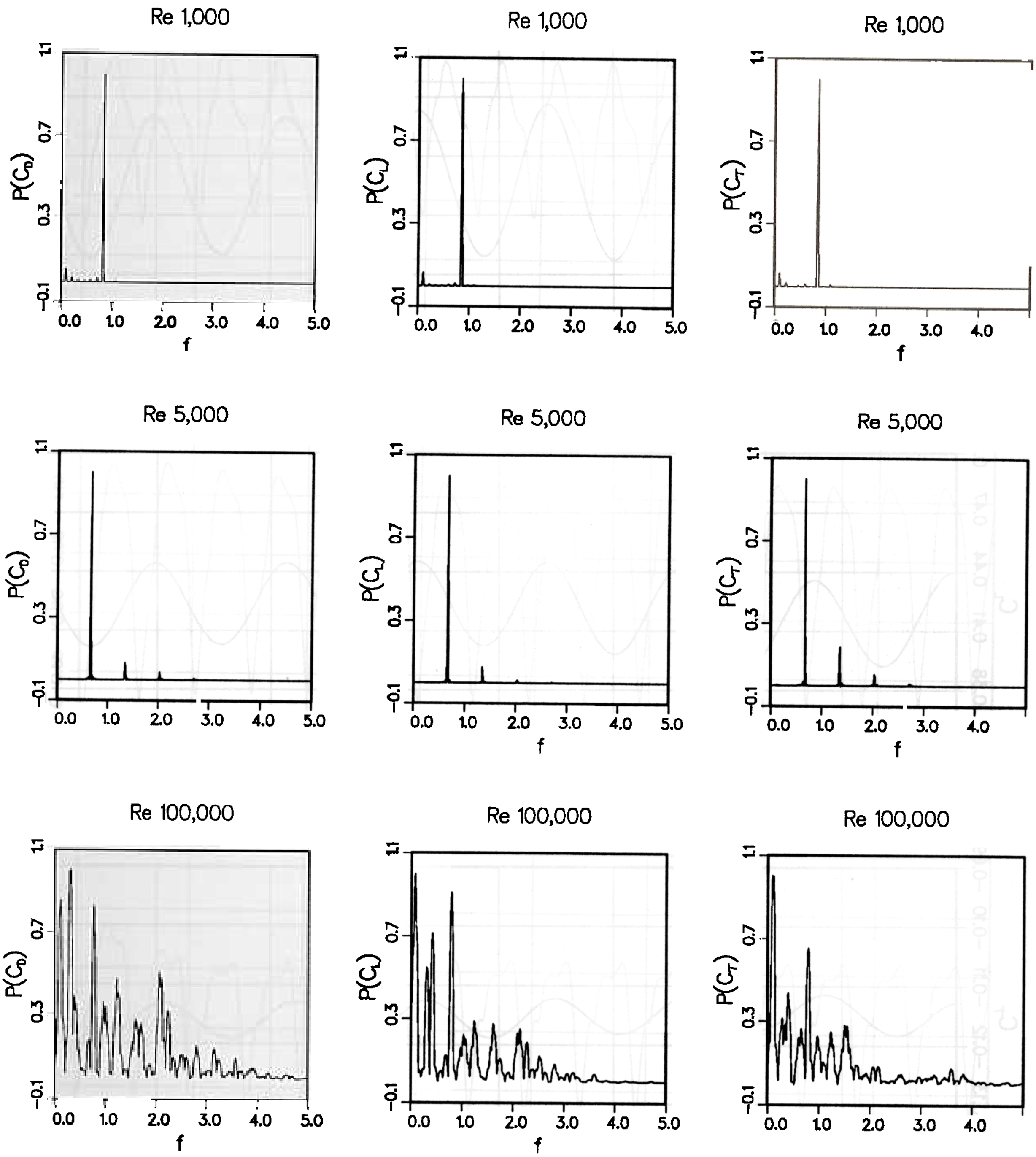

Fig. 6. Flow past a stationary NACA 0012 airfoil: power spectra of the lift, drag and torque coefficients at Re = 1000, 5000 and 100 000.

4.2.2. *Reynolds number 5000*

The mesh and the time step used for this problem is the same as for Reynolds number 1000. Figure 11 shows the time histories of the lift, drag and torque coefficients acting on the airfoil. We observe that the flow eventually reaches a periodic state. When we compare this figure to Figure 7, for Reynolds number 1000, we observe that both the mean values and the magnitudes of the temporally fluctuating components of the aerodynamic coefficients are higher for Reynolds number 5000. This suggests the

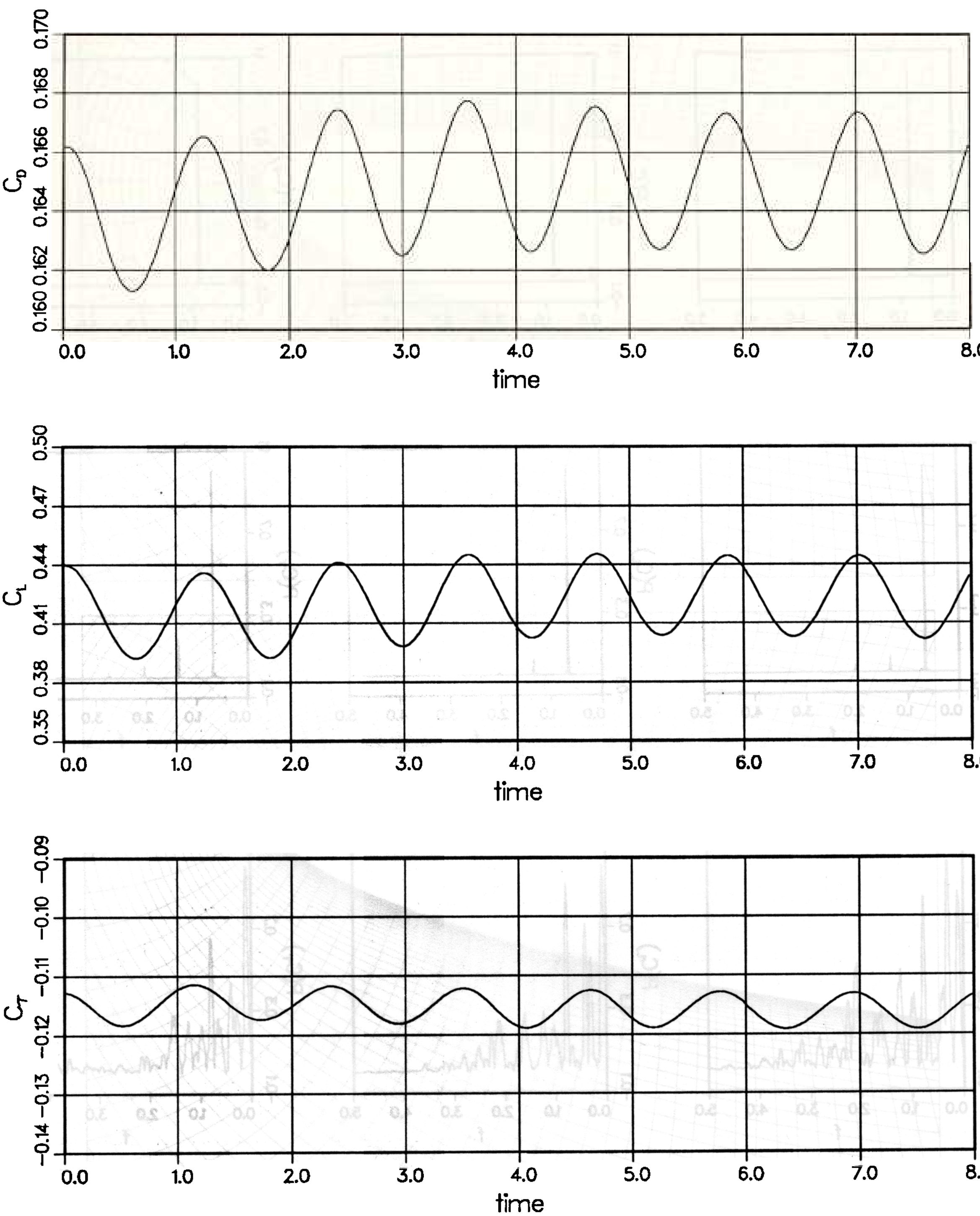

Fig. 7. Flow past a stationary NACA 0012 airfoil at Re = 1000: time histories of the drag, lift and torque coefficients.

presence of stronger vortices on the surface of the airfoil for the Reynolds number 5000 case. This observation is also made when we compare the flow field pictures of the two cases. Figure 12 shows a sequence of frames for the vorticity field during one period of the lift coefficient. The first and last frames correspond to the minimum lift coefficient. The second and fourth frames correspond to the mean value of the lift coefficient, while the third frame corresponds to the maximum value of the left

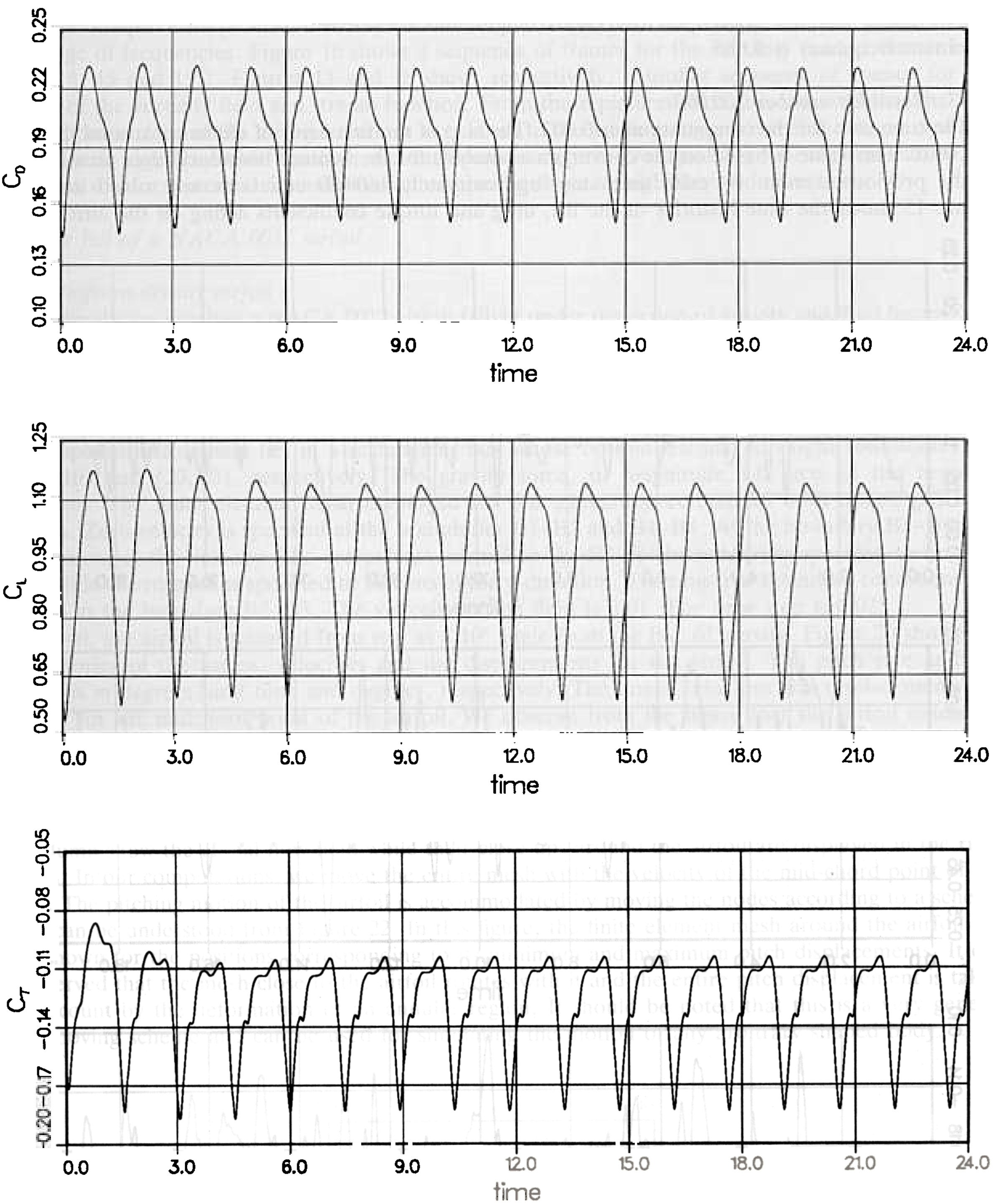

Fig. 11. Flow past a stationary NACA 0012 airfoil at Re = 5000: time histories of the drag, lift and torque coefficients.

coefficient. We notice that there is a significant interaction between the vortices shed from the upper surface and the ones shed from the lower surface of the airfoil. The entire wake with counter-rotating vortices propels itself upwards. Figures 13 and 14 show, respectively, a similar sequence of frames for the close-up of the vorticity field and stream function. From Figure 6 we observe that the flow at Reynolds number 5000 has very weak components at frequencies other than the dominant frequency.

The Strouhal number (based on the chord length and free-stream velocity) corresponding to the dominant frequency is 0.685.

4.2.3. Reynolds number 100 000

The time step for the computations is 0.002. The size of the first layer of elements around the airfoil is 0.0001. This value is based on the convergence analysis for the laminar boundary layer on a flat plate in the previous section. At each time step, approximately 160 000 equations are solved iteratively. Figure 15 shows the time histories of the lift, drag and torque coefficients acting on the airfoil. From

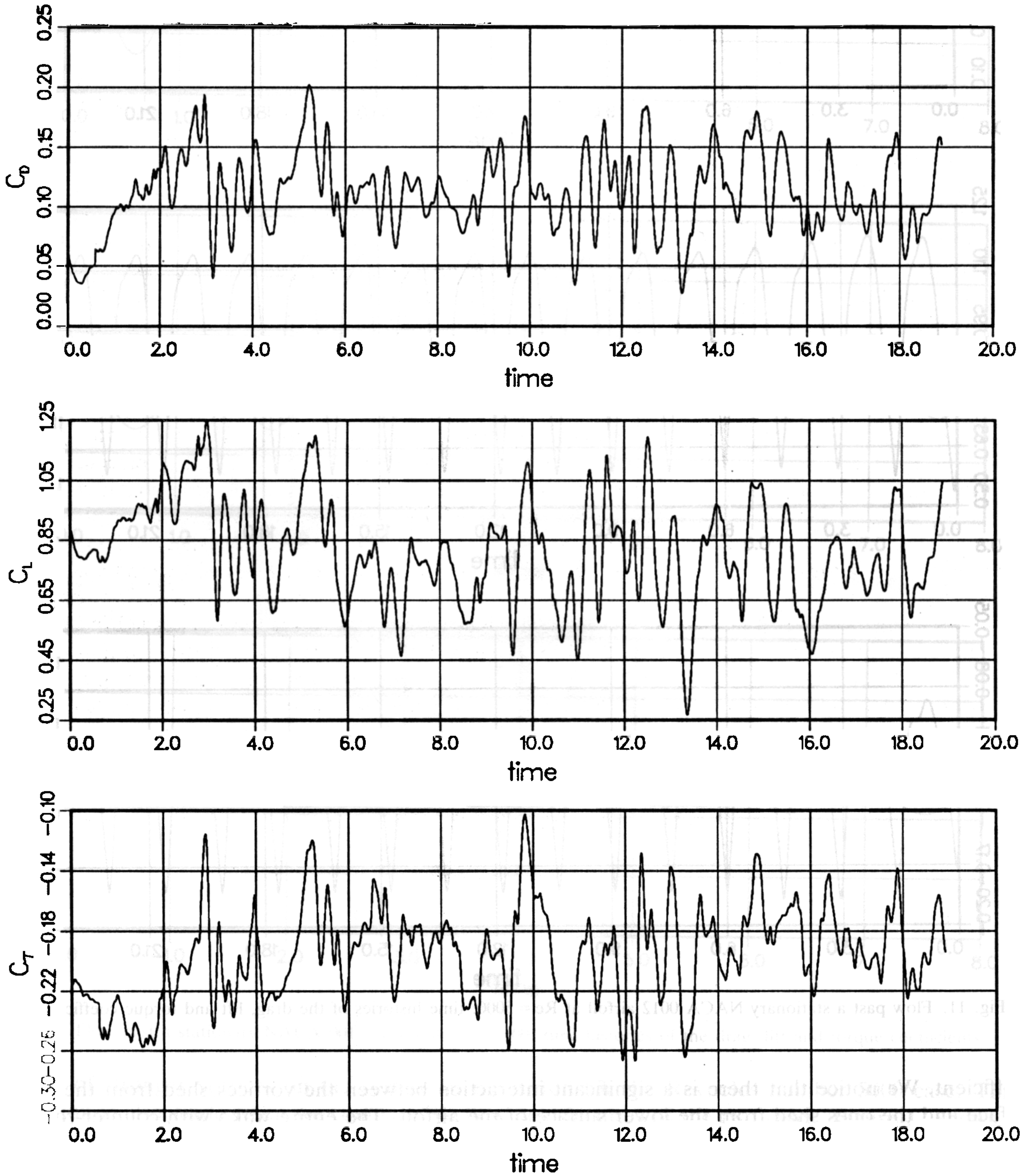

Fig. 15. Flow past a stationary NACA 0012 airfoil at Re = 100 000: time histories of the drag, lift and torque coefficients.

Figure 6 we observe that the flow at Reynolds number 100 000 has components that are spread over a wide range of frequencies. Figure 16 shows a sequence of frames for the vorticity field at time = 14.4, 14.6, 14.8, 15 and 15.2. Figures 17 and 18 show, respectively, a similar sequence of frames for the close-up of the vorticity field and stream function. From these pictures it can be observed that the flow on the upper surface of the airfoil separates very close to the leading edge. We realize that in real life, flows at such high Reynolds numbers are turbulent in nature. Our goal here is to demonstrate the robustness of our numerical formulations in computing flows at high Reynolds numbers.

4.3. *Free fall of a NACA 0012 airfoil*

4.3.1. *Uniform-density airfoil*

This simulation involves a NACA 0012 airfoil falling under the action of gravity and fluid forces. The airfoil is assumed to be made of a material with density 50. The density of the surrounding fluid is 1. Based on the density and the geometry of the airfoil, its mass and polar moment of inertia are, respectively, 4.068 and 0.224. The center of gravity of the airfoil is located at 0.417 chord lengths from the leading edge. The airfoil (marked as 'A' in Fig. 19) of unit-chord-length is initially located at $(0, 0)$. The computational domain lies in a rectangular box whose bottom left and top right coordinates are $(-20, -10)$ and $(20, 20)$, respectively. The gravity force, of magnitude 1.0, acts in the negative y-direction. The finite element mesh employed for this simulation consists of 8446 nodes and 8304 elements. Zero velocity is specified at the boundaries B1–B2 and B1–B4. At the boundary B3–B4, the x component of the velocity (the component normal to the B3–B4 boundary) is specified to be zero value, while the traction is specified to be zero in the y-direction. Traction-free boundary conditions are specified at the boundary B2–B3. The viscosity of the fluid is 0.01. The time step is 0.025.

At $t = 0$, the airfoil is released from rest at a 10° angle from the line of gravity. Figure 20 shows the time histories of the forces, velocities and the displacements for the airfoil. The pitch rate and the rotation is in degrees/unit time and degrees, respectively. The linear velocities and displacements are reported for the midchord point of the airfoil. We observe from the figure that the airfoil reaches a temporally periodic motion. In addition to having a linear velocity, there is a superimposed pitching motion. The average Reynolds number for the periodic solution (based on the linear velocity of the airfoil and its midchord point and its chord length) is, approximately, 225. Figure 21 shows a sequence of frames of the vorticity field at various instants during one pitch cycle of the airfoil. The frames in the left column show the global flow field while their close-ups around the airfoil are displayed in the right column. In our computations, we move the entire mesh with the velocity of the mid-chord point of the airfoil. The pitching motion of the airfoil is accommodated by moving the nodes according to a scheme which can be understood from Figure 22. In this figure, the finite element mesh around the airfoil has been shown for the positions corresponding to its minimum and maximum pitch displacements. It can be observed that the mesh close to the airfoil rotates with it and the entire pitch displacement is taken into account by the deformation of an annular region. It should be noted that this is a very general mesh moving scheme and can be used for simulating the motion of any arbitrary shaped body.

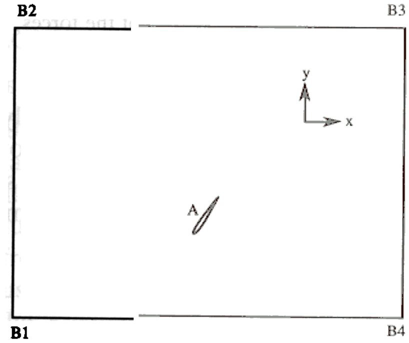

Fig. 19. Free fall of a NACA 0012 airfoil problem description.

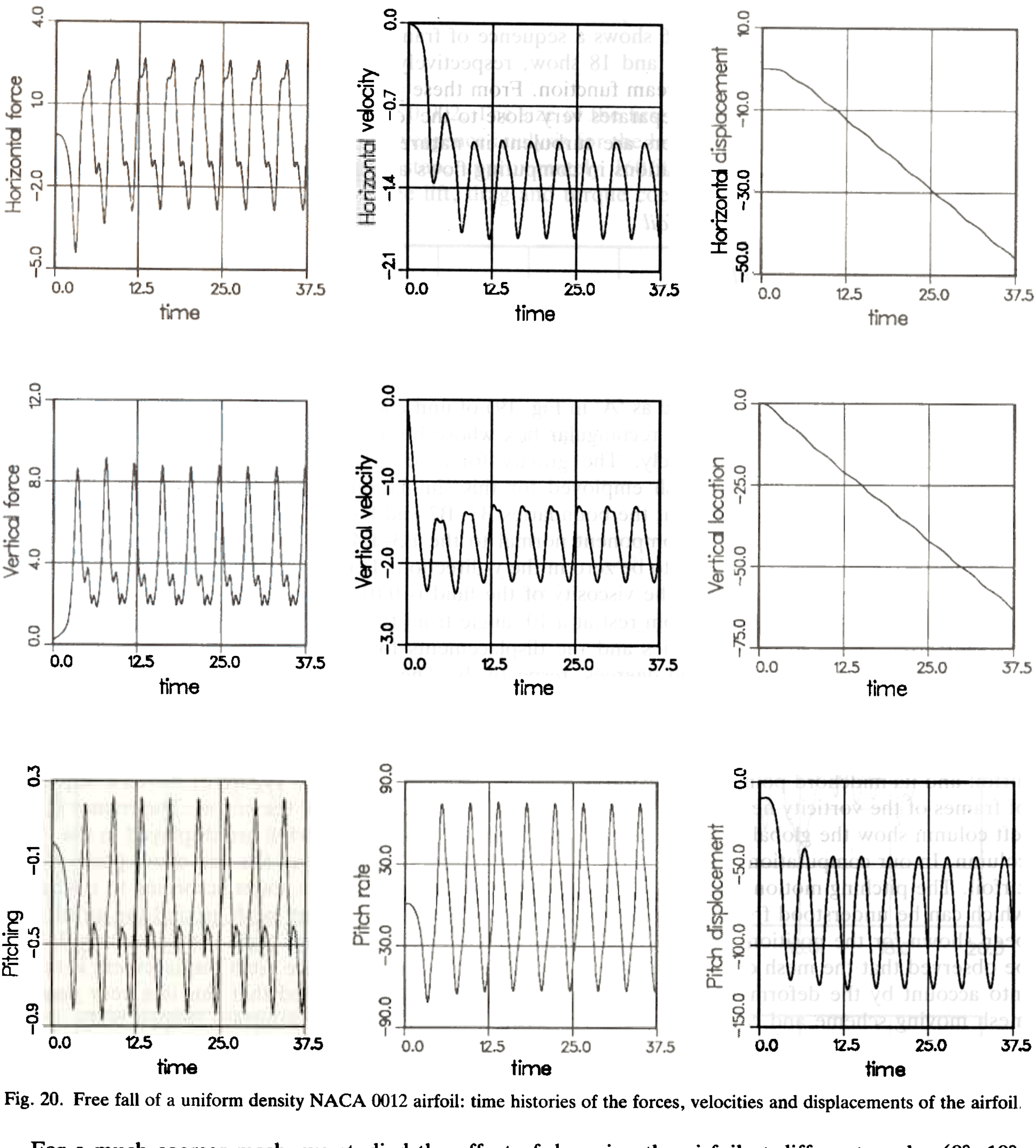

Fig. 20. Free fall of a uniform density NACA 0012 airfoil: time histories of the forces, velocities and displacements of the airfoil.

For a much coarser mesh, we studied the effect of dropping the airfoil at different angles (0°, 10°, 90°) with the vertical. In all the cases we studied, the final, temporally periodic solution obtained is the same. The case when the airfoil is released vertically (i.e., the angle of the airfoil with the vertical is 0°) is very interesting. Initially it travels vertically down. Then, as the speed of the airfoil increases, the vortex shedding begins. Depending on the round-off errors in the computations the airfoil can either go to the right or to the left. In our case, it goes to the left.

4.3.2. Non-uniform density airfoil

This simulation is quite similar to the previous one. This time the mass distribution of the airfoil is not uniform. The nose region of the airfoil, which extends from the leading edge of the airfoil to

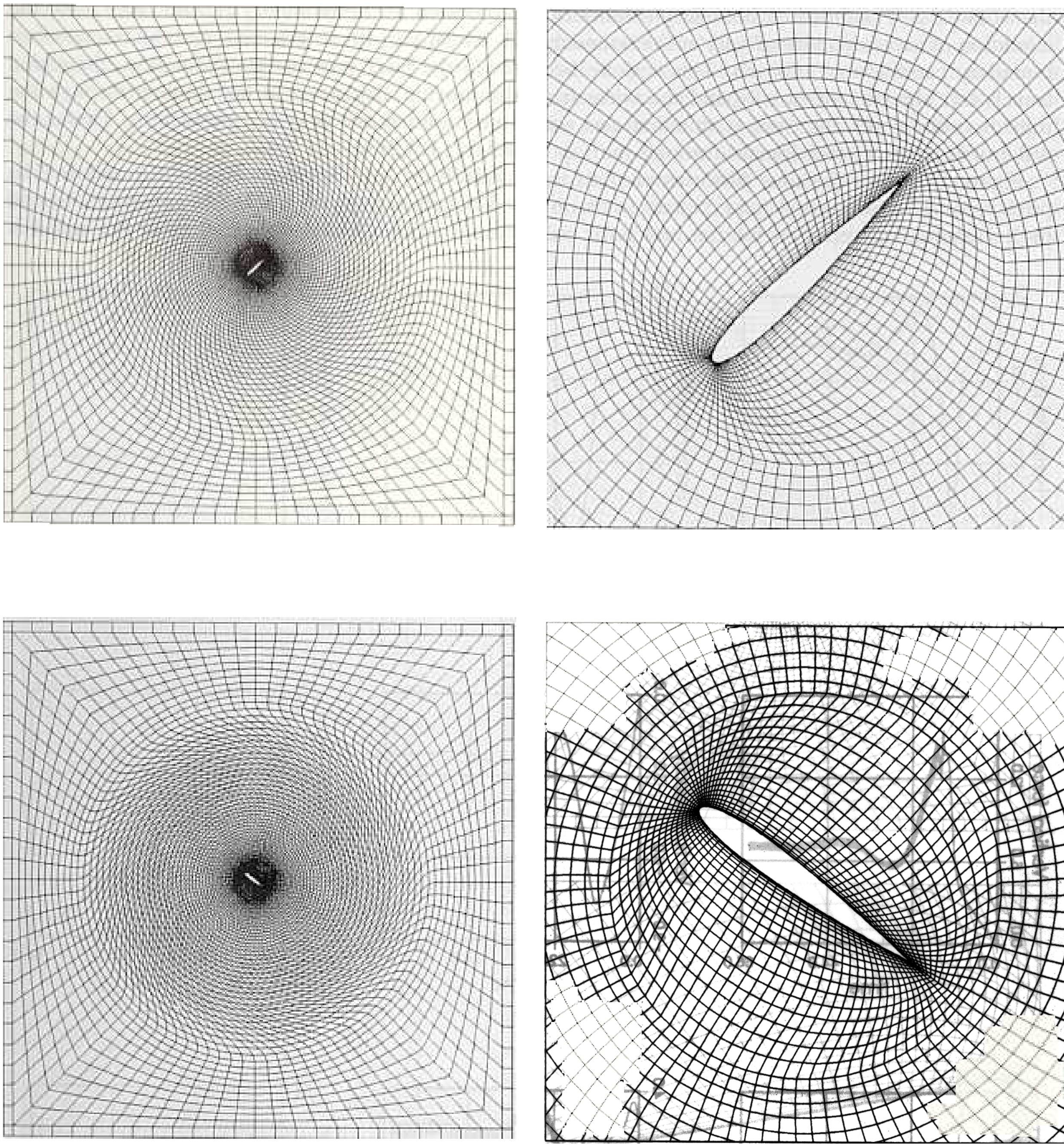

Fig. 22. Free fall of a uniform density NACA 0012 airfoil: finite element mesh close to the airfoil at its minimum and maximum pitch displacements.

one-tenth chord, is of density 500. The density of the remaining airfoil is 50. Based on this density distribution, the mass and the polar moment of inertia on the airfoil are, respectively, 7.05 and 0.448. The center of gravity of the airfoil lies at 0.226 chord lengths from the leading edge. The density and the viscosity of the surrounding fluid are 1.0 and 0.01, respectively.

At $t = 0$, the airfoil is released from rest at a 10° angle with the line of gravity. The mesh employed is the same as the one in the previous problem. Zero velocity is specified at the boundary B1–B4. At the boundaries B1–B2 and B3–B4, the x component of the velocity (the component normal to the two boundaries) is specified to be zero, while the traction is specified to be zero in the direction parallel to the boundary. Traction-free boundary conditions are specified at the boundary B2–B3. At $t = 15$, the condition of no horizontal velocity at the boundary B3–B4 (in Fig. 19) is removed, and the traction-free boundary condition is imposed. This is done because, in the later part of this simulation, the airfoil travels left almost horizontally and the wake from the moving airfoil leaves the domain through the right boundary, B3–B4. Such a situation was not encountered in the previous simulation. There, the wake always leaves the domain through the top boundary, B2–B3.

Figure 23 shows the time histories of the forces, velocities and displacements for the airfoil. The pitch rate and the rotation is in degrees/unit time and degrees, respectively; the linear velocities and displacements are reported for the midchord point of the airfoil. We observe that after the airfoil is

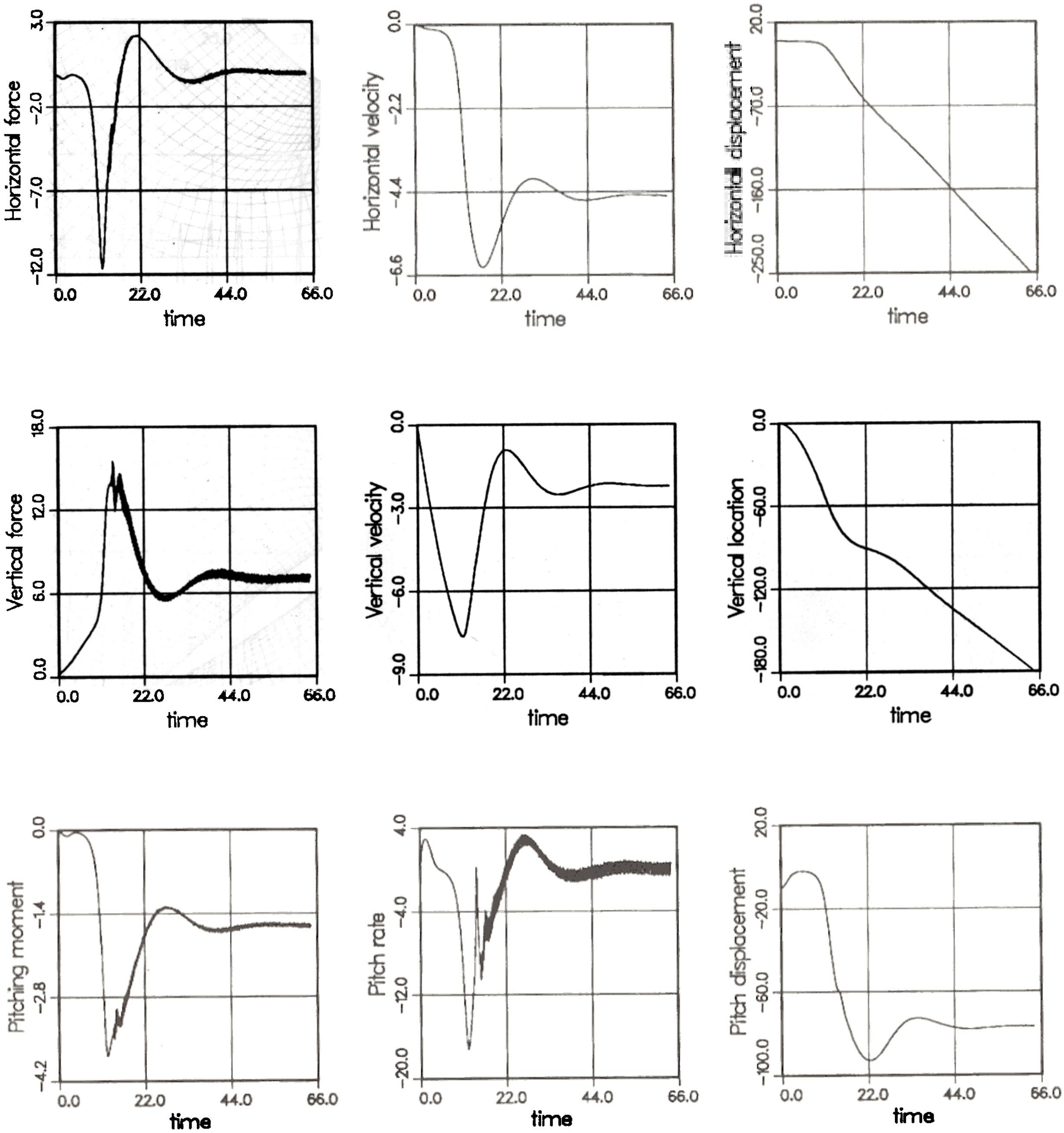

Fig. 23. Free fall of a non-uniform density NACA 0012 airfoil: time histories of the forces, velocities and displacements of the airfoil.

released from rest, it accelerates. At about $t = 12.5$, when the Reynolds number (based on linear velocity of the midpoint of the airfoil) is about 810, the vortex shedding begins. Eventually, the airfoil reaches an almost gliding motion. The Reynolds number is approximately 500. We observe that for this case, the time-varying components of the various quantities related to the airfoil are very small compared to those for the uniform-density airfoil. This can be attributed to the fact that the center of gravity of the present airfoil lies more towards the nose than for the uniform density airfoil. From thin airfoil theory (for inviscid flow), it is well known that the pitch stability of an airfoil increases as the center of gravity moves fore of the aerodynamic center of the airfoil (roughly at quarter chord point of the airfoil); the case in which the center of gravity lies aft of the aerodynamic center is unstable [16].

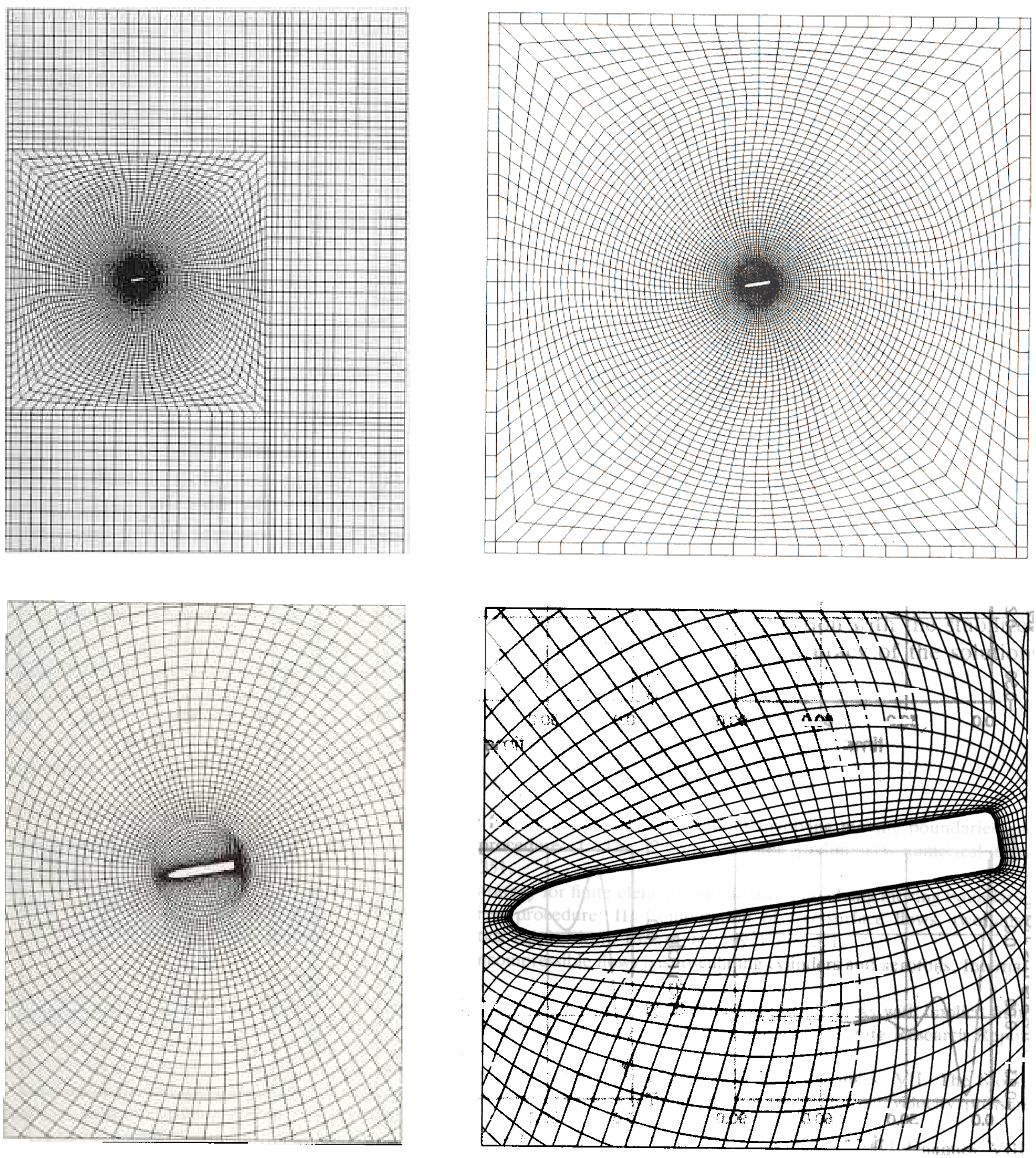

Fig. 25. Dynamics of a projectile: finite element mesh and its detailed views around the projectile.

Figure 24 shows a sequence of frames of the vorticity field and stream function at $t = 15.625$, 23.125, 30.625, 38.125, 45.625 and 53.125.

4.4. *Dynamics of a two-dimensional 'projectile'*

In this problem, we simulate the dynamics of a two-dimensional 'projectile'. The projectile is modeled by a two-dimensional, bullet-like object. The nose section of the projectile, one-fifth of the chord, is a half ellipse. The remaining part of the object is a rectangle with rounded off corners. The maximum thickness of the projectile is 12% of the chord. The finite element mesh used for this problem is very similar to the one in the previous problem. The mesh and its close-up is shown in Fig. 25. The

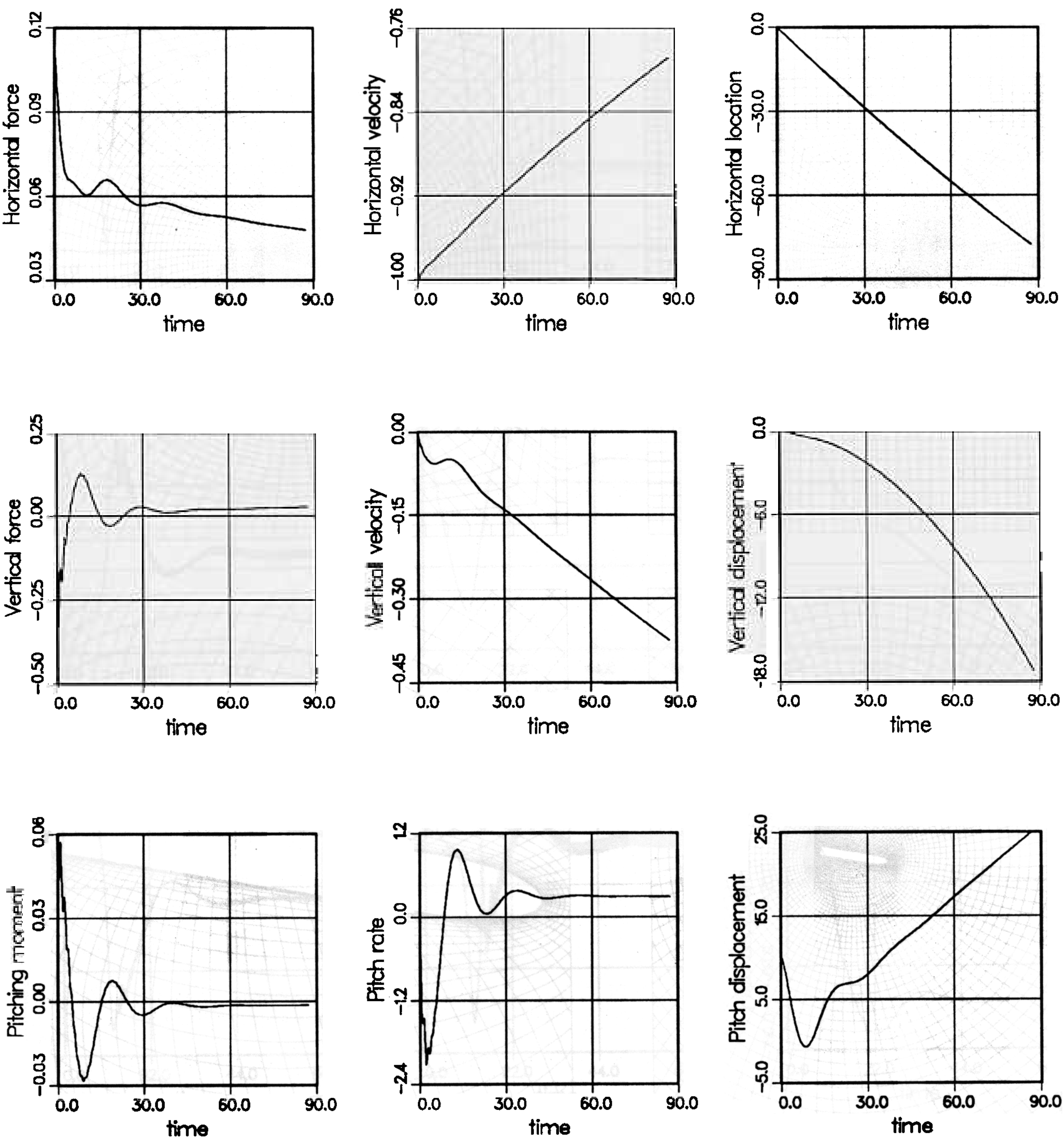

Fig. 26. Dynamics of a projectile: time histories of the forces, velocities and displacements of the airfoil.

density of the nose is 1000 while that of the rest of the object is 50. The density of the surrounding fluid is 1. The mass and polar moment of inertia are, respectively, 23.64 and 1.23. The center of gravity of the projectile lies at 0.21 chord lengths from the leading edge. The gravity force, of magnitude 0.005, acts in the negative y-direction. Zero velocity is specified at the left boundary, B1–B2 (see Fig. 19). At the lower and upper boundaries, B1–B4 and B2–B3, the normal velocity is specified to be zero, with zero traction specified in the tangential direction. Traction-free boundary conditions are specified at the right boundary, B3–B4. The viscosity of the fluid is 0.001. The time step used is 0.025. The initial condition for this simulation is the unsteady solution for flow past the projectile which is being towed at a 10° angle of attack in the negative x-direction at a speed of 1.0. Then the projectile is released. Figure 26 shows the time histories of the forces, velocities and the displacements of the projectile. The pitch rate and rotation is in degrees/unit time and degrees, respectively; the linear velocities and displacements are reported for the midchord point of the projectile. Figure 27 shows a sequence of frames of the vorticity field and stream function at $t = 0$, 17.5, 35, 52.5, 70, 87.5. From these figures we observe that, as the simulation progresses, the magnitude of the vertical component of the velocity increases while that of the horizontal component decreases. As expected, the overall speed of the projectile decreases. Also, the pitch displacement of the projectile increases with time but the angle of attack stays at a value close to zero. This fact can be observed from the stream function pictures.

5. Concluding remarks

Numerical results were presented for unsteady flows involving fluid–body interactions. These computations were carried out on the Thinking Machines CM-200 and CM-5 supercomputers based on the massively parallel implementations of the stabilized space–time finite element formulation. Unsteady flows past a stationary NACA 0012 airfoil were computed for three different Reynolds numbers. Significantly different flow patterns were observed for the three cases. The finite element mesh for flow at Reynolds number 100 000 was determined on the basis of a convergence study for boundary layer on a flat plate. The dynamics of an airfoil falling in viscous fluid under the influence of gravity was studied for two different mass distributions of the airfoil. It was observed that the location of the center of gravity of the airfoil plays an important role in determining its pitch stability. The method was also used to compute the dynamics of a two-dimensional 'projectile' that has a certain initial velocity. The use of specially designed mesh moving schemes in conjunction with the stabilized space–time formulation, to eliminate the need for remeshing, ensures high accuracy of the solutions and aids in the efficient utilization of massively parallel computers.

References

[1] T.E. Tezduyar, M. Behr and J. Liou, A new strategy for finite element computations involving moving boundaries and interfaces – The deforming-spatial-domain/space-time procedure: I. The concept and the preliminary numerical tests, Comput. Methods Appl. Mech. Engrg. 94 (1992) 339–351.

[2] T.E. Tezduyar, M. Behr, S. Mittal and J. Liou, A new strategy for finite element computations involving moving boundaries and interfaces – The deforming-spatial-domain/space-time procedure: II. Computation of free-surface flows, two-liquid flows, and flows with drifting cylinders, Comput. Methods Appl. Mech. Engrg. 94 (1992) 353–371.

[3] S. Mittal and T.E. Tezduyar, A finite element study of incompressible flows past oscillating cylinders and aerofoils, Internat. J. Numer. Methods Fluids 15 (1992) 1073–1118.

[4] M. Behr, A. Johnson, J. Kennedy, S. Mittal and T.E. Tezduyar, Computations of incompressible flows with implicit finite element implementations on the Connection Machine, University of Minnesota Supercomputer Institute Research Report UMSI 92/102, 1992.

[5] T.J.R. Hughes and L.P. Franca, A new finite element formulation for computational fluid dynamics: VII. The Stokes problem with various well-posed boundary conditions: Symmetric formulations that converge for all velocity/pressure spaces, Comput. Methods Appl. Mech Engrg. 65 (1987) 85–96.

[6] T.J.R. Hughes, L.P. Franca and G.M. Hulbert, A new finite element formulation for computational fluid dynamics: VIII. The Galerkin/least-squares method for advective–diffusive equations, Comput. Methods Appl. Mech. Engrg. 73 (1989) 173–189.

[7] F. Shakib, Finite element analysis of the compressible Euler and Navier–Stokes equations, Ph.D. Thesis, Department of Mechanical Engineering, Stanford University, Stanford, CA 1988.
[8] J. Liou and Tezduyar, Clustered element-by-element computations for fluid flow, in: H.D. Simon, ed., Parallel Computational Fluid Dynamics – Implementations and Results, Scientific and Engineering Computation Series (MIT Press, Cambridge, MA, 1992) 167–187.
[9] P. Hansbo and A. Szepessy, A velocity–pressure streamline diffusion finite element method for the incompressible Navier–Stokes equations, Comput. Methods Appl. Mech. Engrg. 84 (1990) 175–192.
[10] Y. Saad and M.H. Schultz, A generalized minimal residual algorithm for solving nonsymmetric linear systems, SIAM J. Sci. Statist. Comput. 7 (1986) 856–869.
[11] A.N. Brooks and T.J.R. Hughes, Streamline upwind/Petrov–Galerkin formulations for convection dominated flows with particular emphasis on incompressible Navier–Stokes equations, Comput. Methods Appl. Mech. Engrg. 32 (1982) 199–259.
[12] T.E. Tezduyar, S. Mittal, S.E. Ray and R. Shih, Incompressible flow computations with stabilized bilinear and linear equal-order-interpolation velocity–pressure elements, Comput. Methods Appl. Mech. Engrg. 95 (1992) 221–242.
[13] H. Schlichting, Boundary Layer Theory, translated by J. Kestin (McGraw-Hill, New York, 1968).
[14] L.P. Franca, S.L. Frey and T.J.R. Hughes, Stabilized finite element methods: I. Application to the advective–diffusive model, Comput. Methods Appl. Mech. Engrg. 95 (1992) 253–276.
[15] L.P. Franca and S.L. Frey, Stabilized finite element methods: II. The incompressible Navier–Stokes equations, Comput. Methods Appl. Mech. Engrg. 99 (1992) 209–233.
[16] C.D. Perkins and R.E. Hage, Airplane Performance Stability and Control (Wiley, New York, 1949).

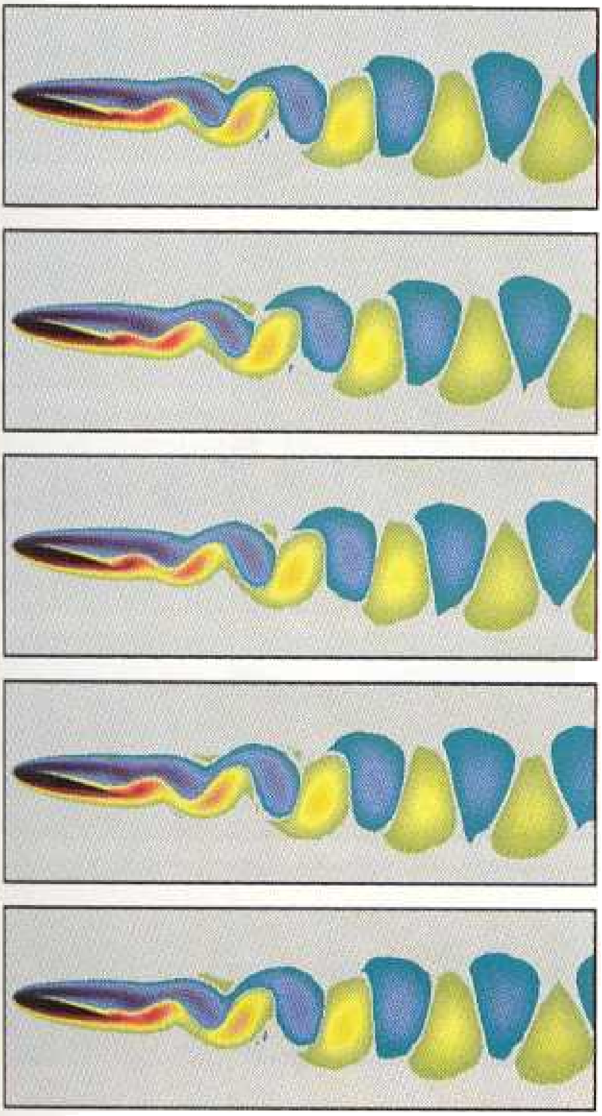

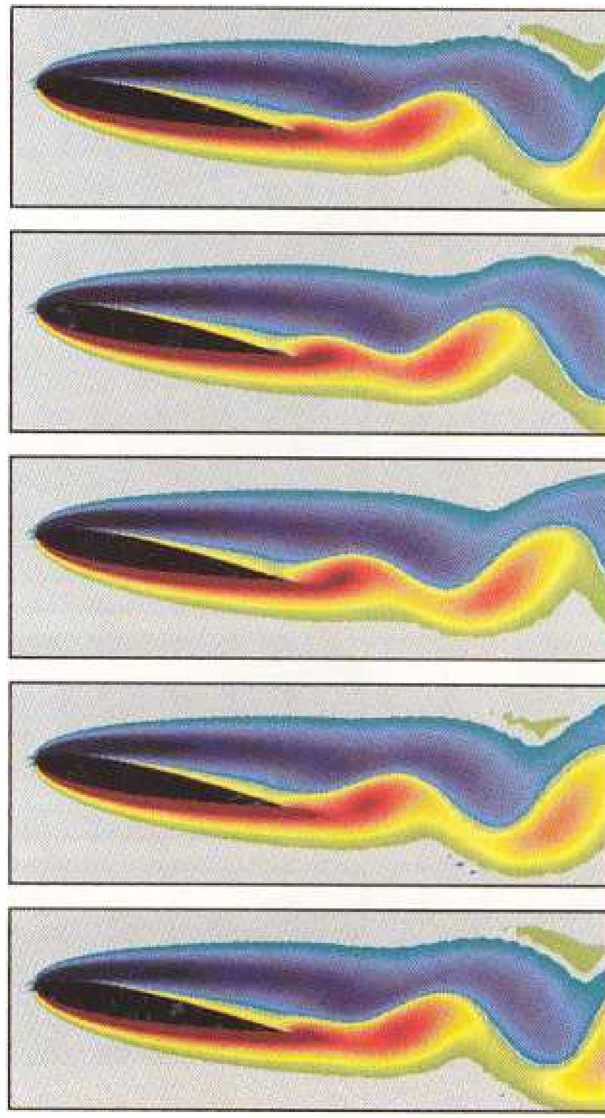

Fig. 8. Flow past a stationary NACA 0012 airfoil at Re = 1000: vorticity at various instants during one period of the lift coefficient.

Fig. 9. Flow past a stationary NACA 0012 airfoil at Re = 1000: detailed view of the vorticity close to airfoil at various instants during one period of the lift coefficient.

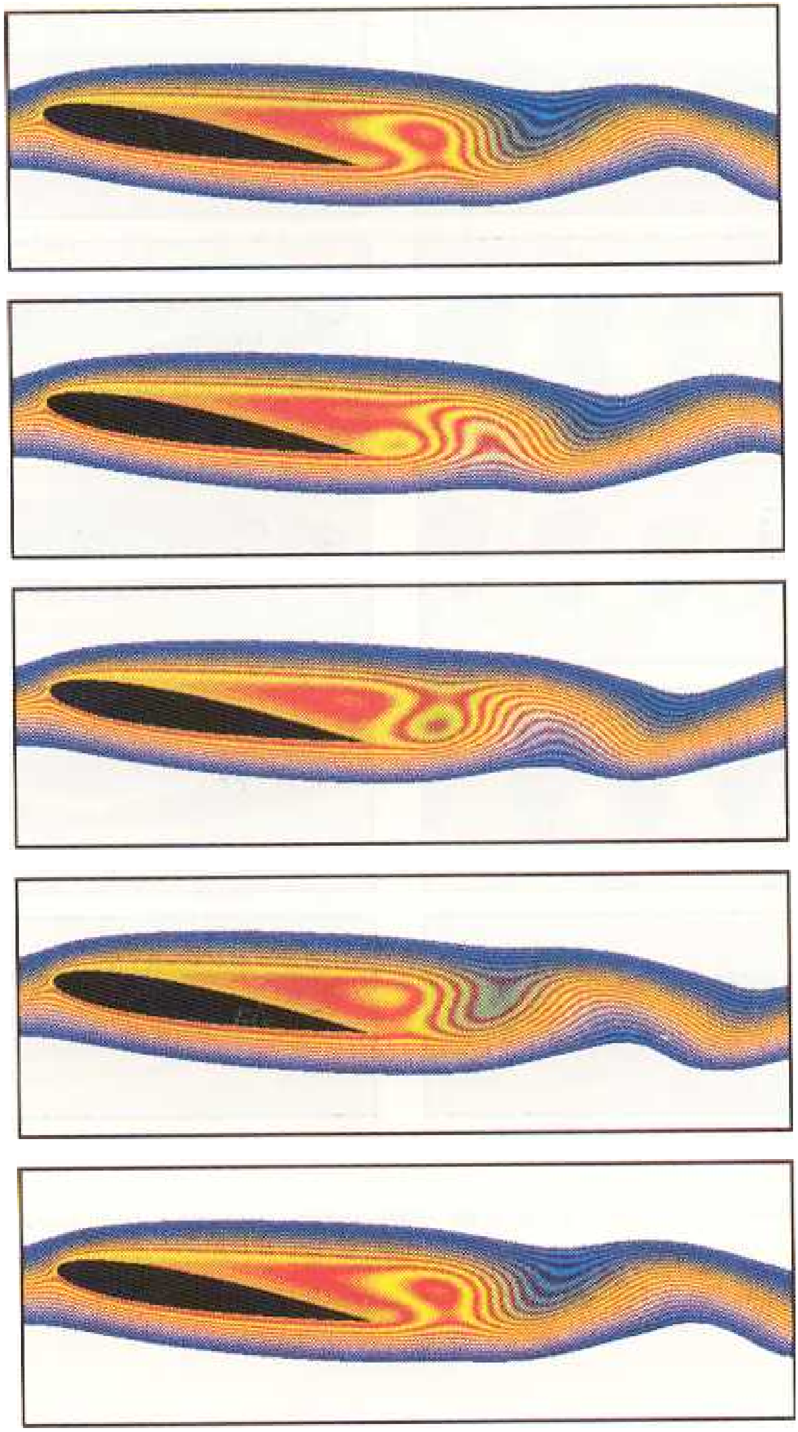

Fig. 10. Flow past a stationary NACA 0012 airfoil at Re = 1000: detailed view of the stream function close to airfoil at various instants during one period of the lift coefficient.

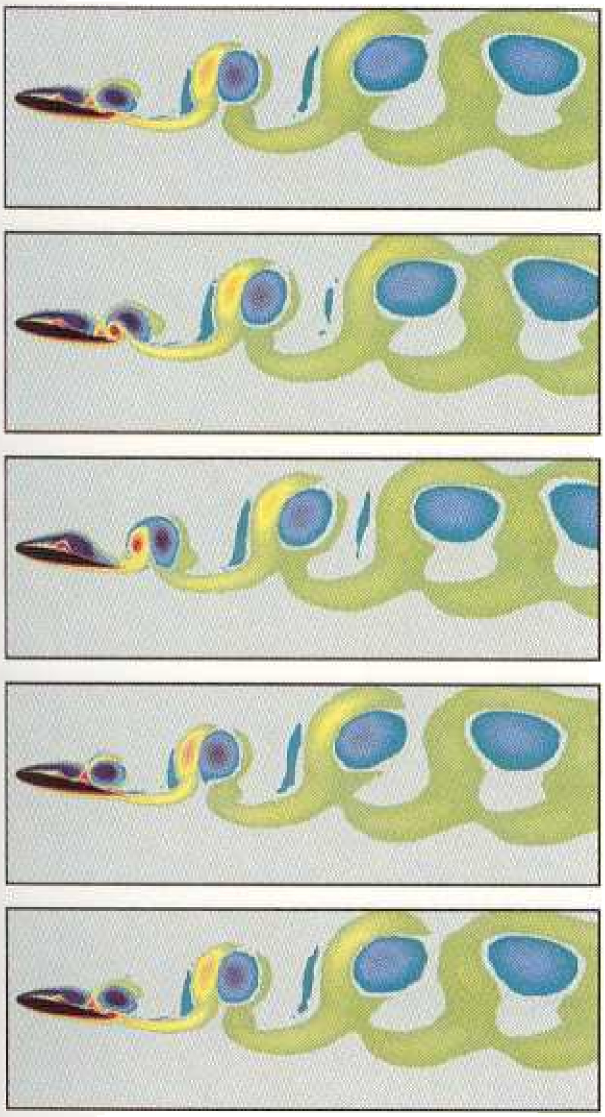

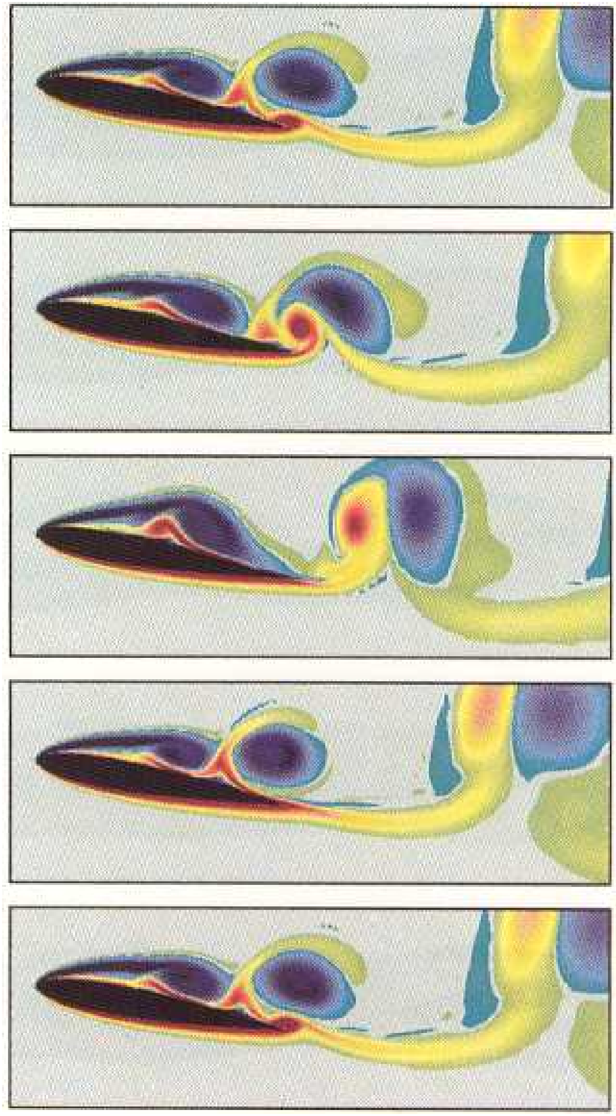

Fig. 12. Flow past a stationary NACA 0012 airfoil at Re = 5000: vorticity at various instants during one period of the lift coefficient.

Fig. 13. Flow past a stationary NACA 0012 airfoil at Re = 5000: detailed view of the vorticity close to airfoil at various instants during one period of the lift coefficient

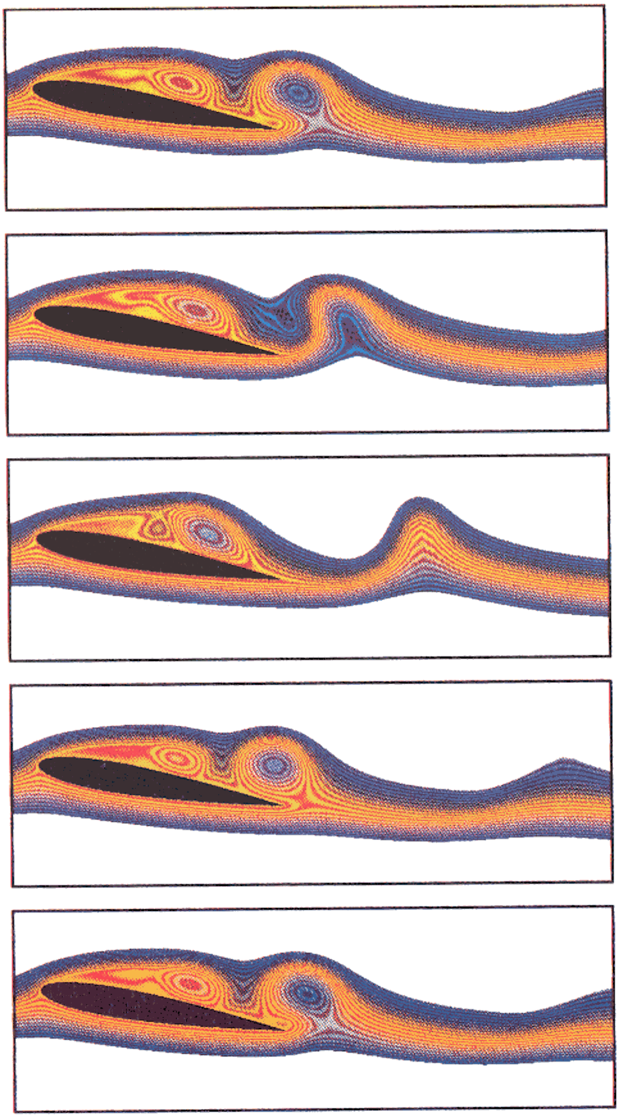

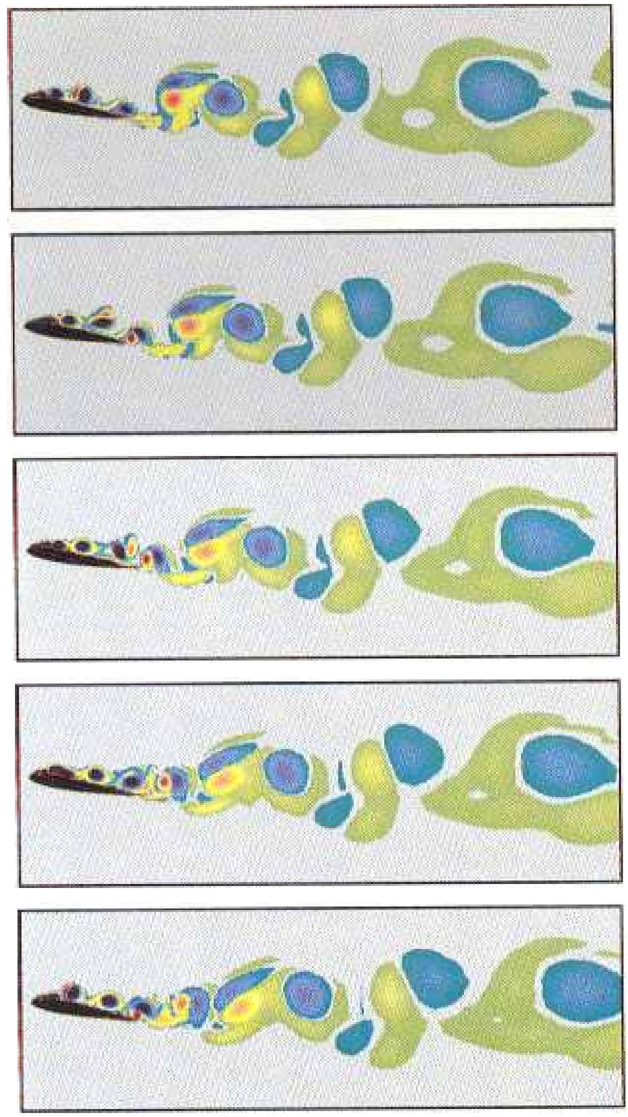

Fig. 14. Flow past a stationary NACA 0012 airfoil at Re = 5000: detailed view of the stream function close to airfoil at various instants during one period of the lift coefficient.

Fig. 16. Flow past a stationary NACA 0012 airfoil at Re 100 000: vorticity at t 14.4, 14.6, 14.8, 15.0 and 15.2.

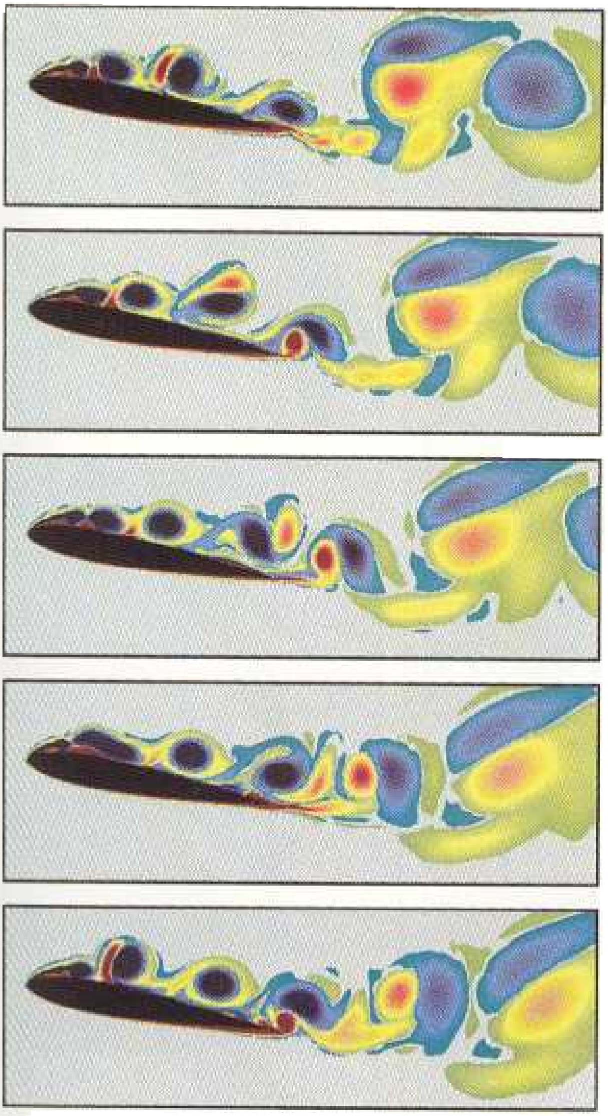

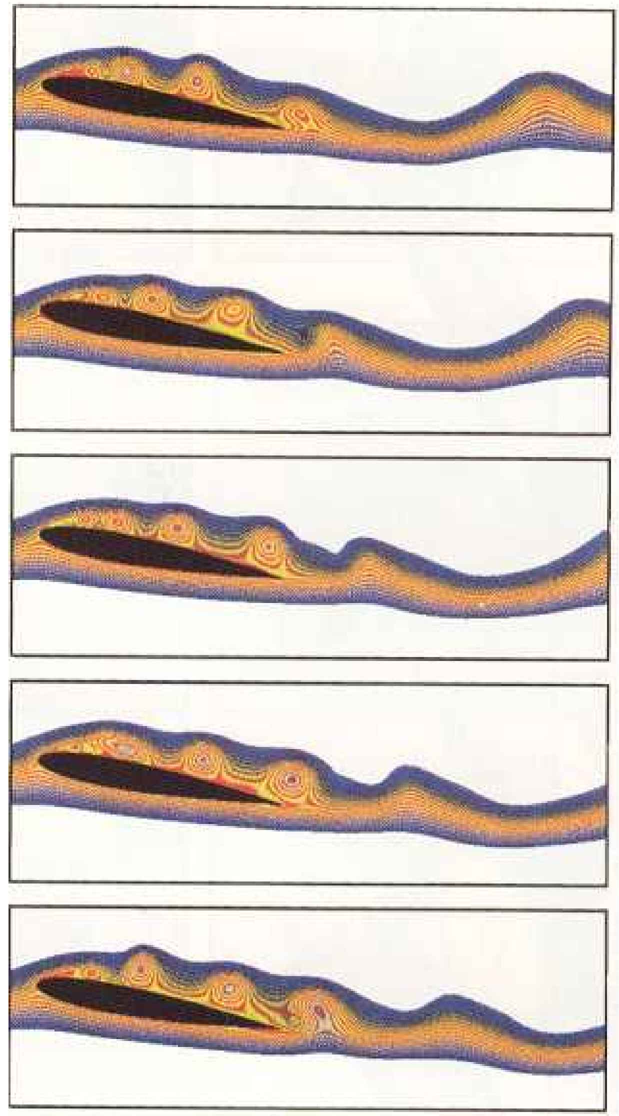

Fig. 17. Flow past a stationary NACA 0012 airfoil at Re = 100 000: detailed view of the vorticity close to airfoil at $t = 14.4$, 14.6, 14.8, 15.0 and 15.2.

Fig. 18. Flow past a stationary NACA 0012 airfoil at Re = 100 000: detailed view of the stream function close to airfoil at $t = 14.4$, 14.6, 14.8, 15.0 and 15.2.

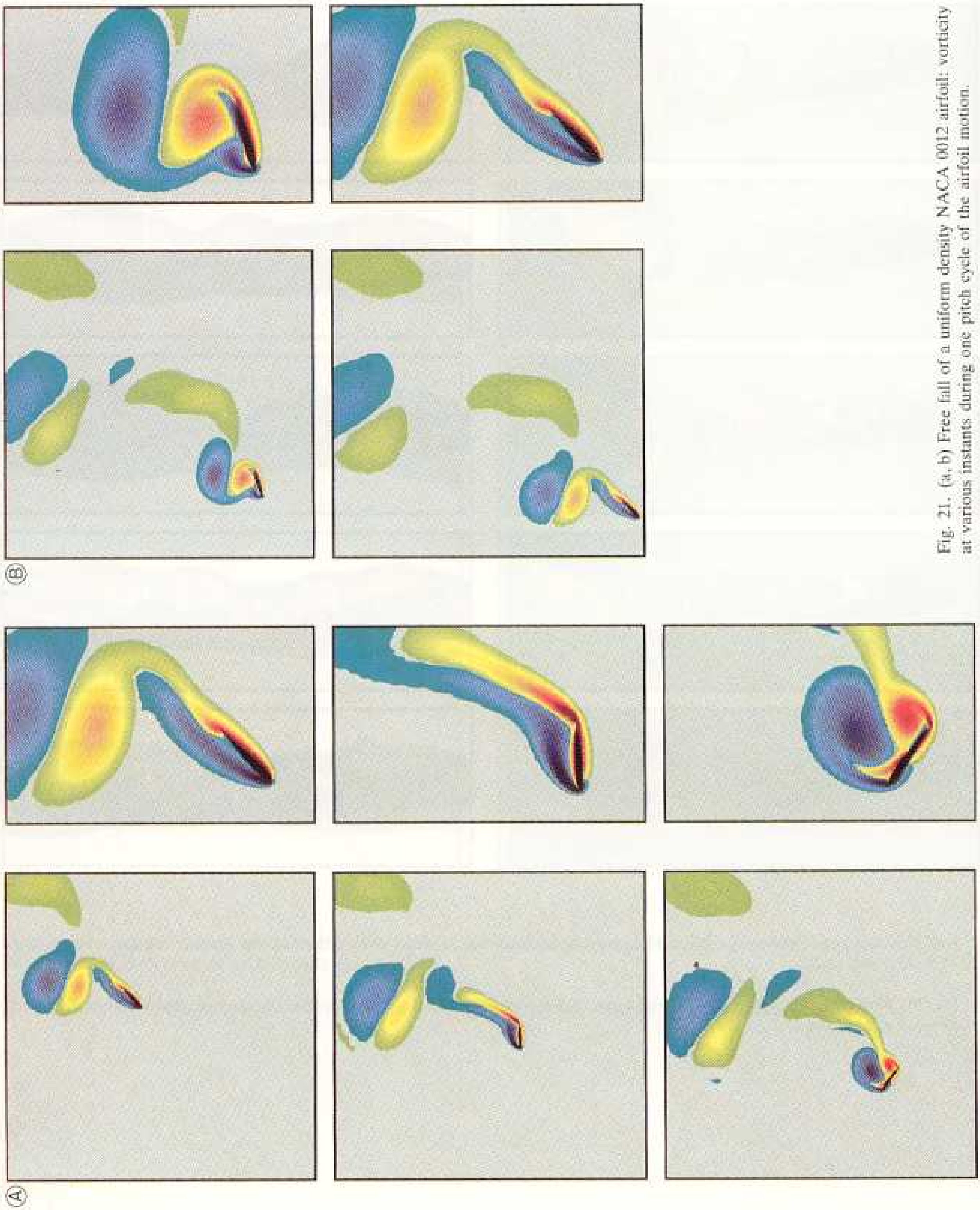

Fig. 21. (a, b) Free fall of a uniform density NACA 0012 airfoil: vorticity at various instants during one pitch cycle of the airfoil motion.

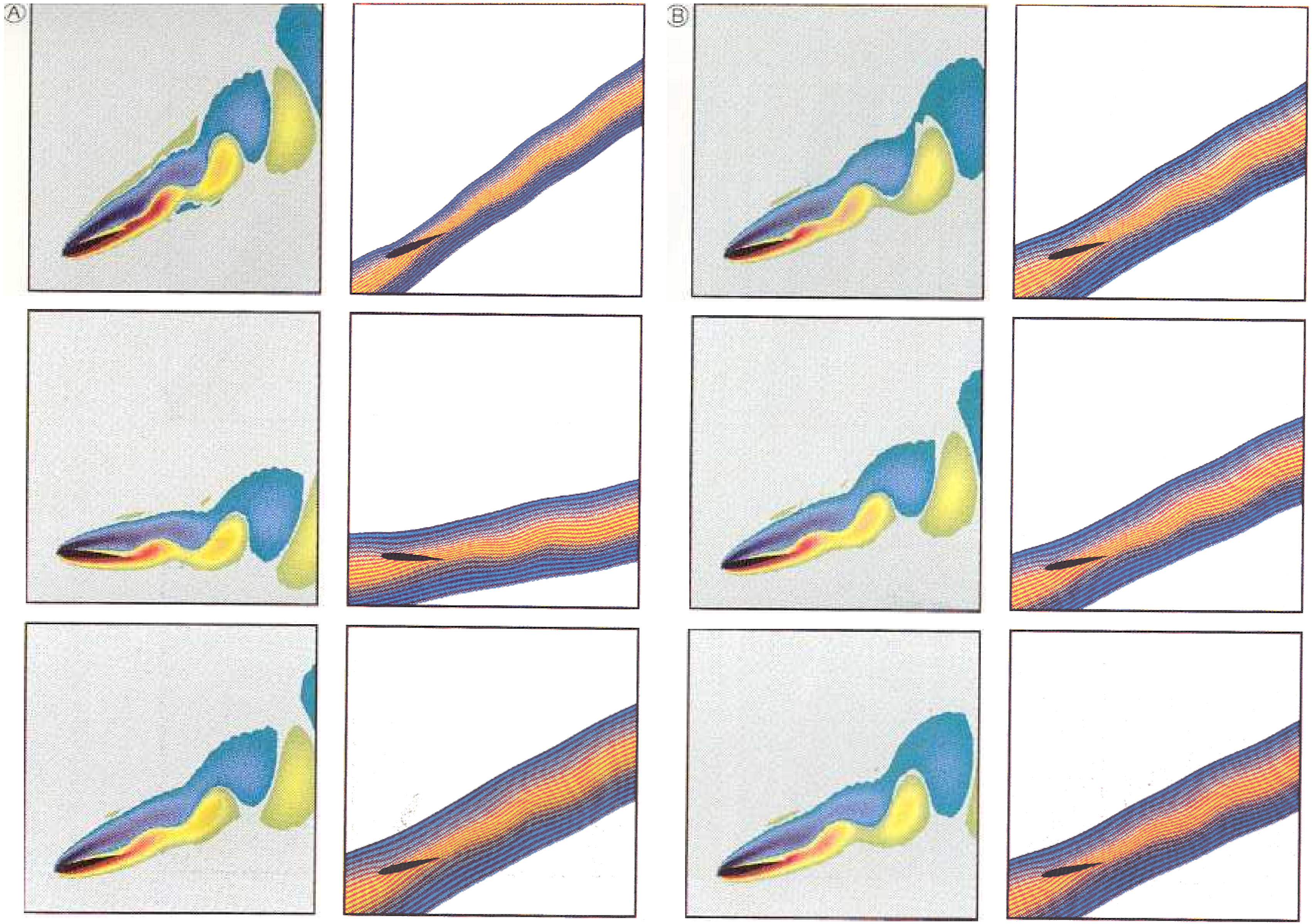

Fig. 24. Free fall of a non-uniform density NACA 0012 airfoil: vorticity (left) and stream function (right) at (a) $t = 15.625$, 23.125 and 30.625, (b) $t = 38.125$, 45.625 and 53.125.

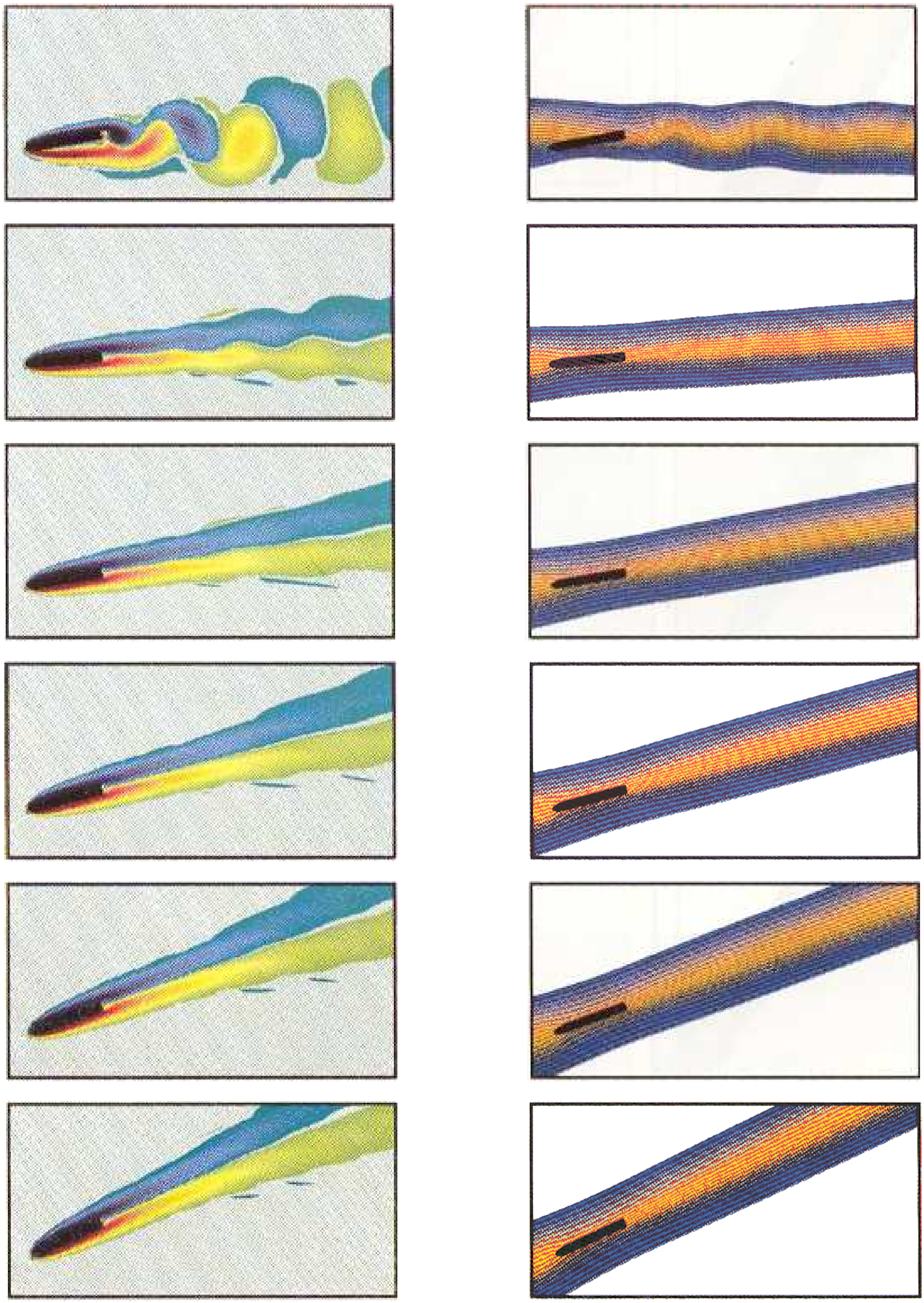

Fig. 27. Dynamics of a two-dimensional 'projectile': vorticity (left) and stream function (right) at $t = 0$, 17.5, 35.5, 52.5, 70 and 87.5.